A Nonlinear Interface Element for 3D Mesoscale Analysis of Brick-Masonry Structures

L. Macorini[1], B.A. Izzuddin[2]

Abstract

This paper presents a novel interface element for the geometric and material nonlinear analysis of unreinforced brick-masonry structures. In the proposed modelling approach, the blocks are modelled using 3D continuum solid elements, while the mortar and brick-mortar interfaces are modelled by means of the 2D nonlinear interface element. This enables the representation of any 3D arrangement for brick-masonry, accounting for the in-plane stacking mode and the through-thickness geometry, and importantly it allows the investigation of both the in-plane and the out-of-plane response of unreinforced masonry panels. A co-rotational approach is employed for the interface element, which shifts the treatment of geometric nonlinearity to the level of discrete entities, and enables the consideration of material nonlinearity within a simplified local framework employing first-order kinematics. In this respect, the internal interface forces are modelled by means of elasto-plastic material laws based on work-softening plasticity and employing multi-surface plasticity concepts. Following the presentation of the interface element formulation details, several experimental-numerical comparisons are provided for the in-plane and out-of-plane static behaviour of brick-masonry panels. The favourable results achieved demonstrate the accuracy and the significant potential of using the developed interface element for the nonlinear analysis of brick-masonry structures under extreme loading conditions.

Keywords: non linear interface element, cohesive model, multi-surface plasticity, geometric nonlinearity, brick-masonry, in-plane and out-of-plane behaviour.

[1] Marie Curie Research Fellow, Department of Civil and Environmental Engineering, Imperial College London.
[2] Professor of Computational Structural Mechanics, Department of Civil and Environmental Engineering, Imperial College London.

Introduction

Nonlinear interface elements represent an effective tool to model interaction among different constitutive components of solids and to capture failure mechanisms in a large variety of structural systems. Interface elements were initially employed for simulating discontinuities in rock mechanics [1] and cracks in brittle materials like concrete [2], while more recently they have been used to model delamination and fracture in multi-layered composites [3,4].

In order to accurately reproduce most of the physical phenomena associated with interface failure, the interface elements have to be coupled with accurate material models that relate tractions with separation displacements. Some main features of such constitutive relations were introduced in the first cohesive zone models tailored to analyse crack propagation in either ductile or brittle materials (a detailed review can be found in [5]). At present, the most advanced cohesive models are based on either softening plasticity [6] or damage mechanics [7]. They account for the interaction between opening and sliding fracture modes and allow the description of delamination, decohesion and loss of friction at the interfaces between different bodies and at the fracture process zones in solid elements.

The use of interface elements is particularly effective when the locus of potential damage and fracture is known a priori, which is typically related to the inherent texture of the analysed structure. This is the case for unreinforced brick-masonry (URM) where bricks are arranged in an orderly manner so as to form structural elements. Experimental outcomes [8] and inspection of failure modes of real URM structures show that cracks usually run along brick-mortar interfaces and can then continue through bricks following continuous paths. These intrinsic features of the brick-masonry structural behaviour suggested the use of nonlinear interface elements for detailed finite element analyses of URM panels under monotonic and cyclic loads [9,10]. In such structural models zero-thickness interfaces are employed to represent the nonlinear behaviour of mortar and brick-mortar interface as well as potential

cracks in bricks. Damage and fracture are assumed to occur at the interfaces only, whereas the connected continuous elements are characterized by a linear elastic behaviour.

Most of the mesoscale models for URM developed so far, account for the in-plane stacking mode of bricks and mortar only, and are aimed at investigating the in-plane nonlinear response of masonry walls. Such models cannot be effectively employed to assess the structural performance under complex loading conditions as in the case of earthquakes, when panels in URM buildings are loaded simultaneously by both in-plane and out-of-plane actions.

In order to define more general analysis tools for mesoscale analysis of URM elements characterized by complex brick arrangements (quarry masonry, multi-leaf walls, etc.), both the in-plane stacking mode and the through-thickness geometry should be represented. Just a few models, presented very recently, consider a detailed description for the 3D texture of URM. These advanced models are based either on the use of the finite element (FE) continuum approach, where the progressive failure is examined at the level of constituents employing solid elements [11] or using 3D kinematic FE limit analysis [12]. The use of the former strategy is typically applicable to only small representative volume elements (RVEs) of masonry, because of the extremely high computational cost, while the latter provides a good approximation for the URM maximum capacity but does not represent all the main structural response features (initial stiffness, progressive damage, post-peak behaviour etc.).

In addition, the aforementioned models account for only material nonlinearity, and do not consider geometric nonlinearity, such as due to large displacements which can be relevant especially when analysing the out of plane behaviour of URM panels. This was confirmed in recent tests [13] that showed how the out-of-plane failure can be governed by geometric instabilities that arise when the URM walls rock out-of-plane under dynamic loads.

A novel 2D nonlinear interface element is presented in this work, which is used in an accurate mesoscale description for the geometric and material nonlinear analysis of URM structures. After presenting the main features of the 3D mesoscale approach for modelling URM structures, the formulation of the 2D nonlinear interface element is detailed. A corotational approach is used to account for geometric nonlinearity, and a multi-surface softening plasticity model is employed to model all the relevant failure modes: opening in tension, sliding in shear/tension and shear/compression and crushing in compression.

In order to demonstrate the applicability and accuracy of the proposed modelling approach, several studies are undertaken on masonry panels in the final part of the paper, where favourable comparisons are achieved between experimental outcomes and numerical predictions.

1. 3D mesoscale model for brick-masonry

In this work, the finite element method is used for mesoscale analysis of URM structures. Adopting a similar approach to that developed by Lourenço & Rots [9] for the in-plane static analysis of single-leaf masonry panels, the blocks are modelled using continuous elements while the mortar and the brick-mortar interfaces are modelled by means of nonlinear interface elements. Furthermore, zero-thickness interface elements are also arranged in the vertical mid-plane of all blocks along the direction of the shorter horizontal dimension so as to account for possible unit failure in tension and shear (Fig. 1). While Lourenço & Rots [9] used linear 2D planar elements for bricks with nonlinear 1D interface elements, the proposed approach utilises 20-noded 3D elastic continuum solid elements and 16-noded 2D nonlinear interface elements, both accounting for large displacements (Fig. 2). This allows the representation of any 3D arrangement for brick-masonry and to model both initial and damage induced anisotropy.

The material nonlinearity that marks the behaviour of bricks, mortar and brick-mortar interfaces is represented through the discrete approach founded on the principles of nonlinear fracture mechanics [5]. The use of nonlinear interface elements to model potential crack or slip planes, allows increased accuracy of the numerical solution simply through mesh refinement [6]. In the present context, the softening post-peak behaviour does not lead to mesh-dependency, since it is directly related to the fracture energy which is an intrinsic material property. This avoids the need for addressing the localisation of the solution that usually arises when the continuum approach featuring smeared-cracking models with softening laws is used [11,14].

However special attention should be paid to determining the global solution because of the brittle nature of the interface model. When cracks develop and spread along the structure, the elastic energy stored in the bulk material connected to a damaged interface has to be redistributed into other elements, leading in certain cases to very sharp snap-backs and solution jumps in the static global response [15]. Specific numerical techniques based on the arc-length method [16] can be used to successfully capture the actual global behaviour. In any case, the use of a fine mesh often allows the determination of a smoother solution, and dynamic analysis techniques can help overcome much of the numerical problems because the suddenly released elastic energy is gradually transformed into kinetic and viscous energy.

According to the finite element method, the boundary value problem for any URM mesoscale model corresponds to a set of local and global nonlinear equations. The local evolution equations are functions of internal variables and define the central problem of computational plasticity at quadrature point level [17], while the global algebraic equations express the equilibrium conditions. The numerical solution is obtained using an incremental-iterative strategy and the backward Euler scheme at local level. At each time or pseudo-time increment, in the case of either dynamic or static analysis respectively, the computation is

performed sequentially in two phases, first the global then the local phase. The displacement approach is used and the displacement increments, the primary variables, are calculated in the global phase and passed to the local phase to solve the plasticity problem. Once the final values of internal variable (stresses, plastic variables etc.) have been determined in the local phase, the internal force vector and the consistent stiffness matrix are obtained. The equilibrium conditions are then checked globally, and, if required, an iterative correction for the displacement increments is performed.

The solution procedure is sketched in Fig. 3, where the nonlinear interface element contribution is shown at time increment n and global iteration k. The global displacements $\boldsymbol{U}$ are transformed into local element nodal displacement $\boldsymbol{d}^e$ first and then into local deformations $\boldsymbol{u}$ at integration point level. Here the central problem in computational plasticity is solved using an iterative strategy, and the stresses $\boldsymbol{\sigma}$ and the corresponding tangent modulus matix $\boldsymbol{k}$ are determined. These are then integrated over the element using the virtual work principle, and the resulting global element nodal resistance forces and tangent stiffness matrix are assembled into the corresponding global structural entities $\boldsymbol{R}$ and $\boldsymbol{K}$. With the applied external loads $\boldsymbol{P}$ known, the out-of-balance between $\boldsymbol{R}$ and $\boldsymbol{P}_n$ determines whether equilibrium has been achieved, and can be used along with $\boldsymbol{K}$ for a subsequent iterative approximation of $\boldsymbol{U}$ if necessary.

With regard to the resistance forces and consistent stiffness matrix for the 20-noded solid elements, these are determined using standard finite element techniques [18,19], considering linear elastic material behaviour based on Green's strain, which allows a simple treatment of geometric nonlinearity in 3D solid elements undergoing small strains.

2. Nonlinear interface element

The proposed interface element, which accounts for both geometric and material nonlinearity, features 16-nodes with 3 translational freedoms for each node: nodes 1-8 lie on the top face of the element, whereas nodes 9-16 lie on the bottom face. As shown in Fig. 4, the two faces, which correspond either to the faces of two solid elements bound through a mortar layer or to adjacent faces of solid elements for a single brick, are coincident in the undeformed configuration. In order to account for large displacements that could characterise the behaviour of interfaces at failure in actual URM panels, a co-rotational approach is employed, and a local reference system that moves with the interface mid-plane is defined. The internal contact forces through the interface are simulated by means of a multi-surface plasticity criterion. An elasto-plastic contact law which follows a Coulomb slip criterion is used to model failure in tension and shear, while a cap model is employed to account for crushing in compression. A formulation that considers energy dissipation, decohesion and residual frictional behaviour has been developed. Moreover a non-associated plastic flow has been introduced for modelling inelastic deformation due to shear. A specific plastic potential, different from the yield function in tension and shear, has been defined to account for the actual dilatancy which is due to the roughness of the fractured shear surface.

2.1. Kinematics and Co-rotational Approach

The co-rotational approach is employed for the large displacement formulation of the 2D interface element. According to this approach, the effects due to geometric nonlinearity can be established through transformations between global and local entities, allowing the use of linear kinematics on the local level, thus shifting the treatment of geometric nonlinearity from the continuum to the discrete level. Denoting the fixed global reference system as (O,X,Y,Z), the local co-rotational reference system (o,x,y,z) follows the element current deformed

configuration (Fig. 4). In particular, relations between global displacements and local deformations, between local and global resistance forces and between local and global tangent stiffness have to be defined [20]. A main issue in any co-rotational approach relates to the choice of an effective local reference system. In this work, the local reference system for the 2D interface element is defined considering the mid-surface between the two joining faces: the local x- and y-axes correspond to the bisector of the elements diagonal of the mid-plane in the deformed configuration. This definition for the local axes satisfies the orthogonality requirements for the two planar axes and supplies a local reference system that is invariant to the specified order of the element nodes [20].

The triad ($\boldsymbol{c}_x$,$\boldsymbol{c}_y$,$\boldsymbol{c}_z$) that defines the orientation of the local system can be obtained from the nodal global displacements $\boldsymbol{U}^e$:

$$\boldsymbol{U}_i^e = \left\langle U_X, U_Y, U_Z \right\rangle_i^{eT} \quad (i = 1,16) \tag{1}$$

$$\boldsymbol{c}_x = \frac{\boldsymbol{c}_{13} - \boldsymbol{c}_{24}}{\left|\boldsymbol{c}_{13} - \boldsymbol{c}_{24}\right|}; \quad \boldsymbol{c}_y = \frac{\boldsymbol{c}_{13} + \boldsymbol{c}_{24}}{\left|\boldsymbol{c}_{13} + \boldsymbol{c}_{24}\right|}; \quad \boldsymbol{c}_z = \boldsymbol{c}_x \times \boldsymbol{c}_y \tag{2}$$

with

$$\boldsymbol{c}_{ij} = \frac{\boldsymbol{v}_{ij}}{\left|\boldsymbol{v}_{ij}\right|} \quad (i = 1,2 \text{ and } j = i+2) \tag{3}$$

$$\boldsymbol{v}_{ij} = \boldsymbol{v}_{ij}^0 + \frac{(\boldsymbol{U}_i^e + \boldsymbol{U}_{i+8}^e)}{2} - \frac{(\boldsymbol{U}_j^e + \boldsymbol{U}_{j+8}^e)}{2} \quad (i = 1,2 \text{ and } j = i+2) \tag{4}$$

where $\boldsymbol{v}_{ij}^0$ correspond to the vector that connects node i to node j in the initial undeformed configuration when the two faces are coincident (Fig. 4).

The transformation from global displacements to local deformations $\boldsymbol{d}^e$, which correspond to the relative displacements between the top and the bottom face in the local reference system, can be performed considering the matrix $\boldsymbol{r}$ that contains the local system normalized vectors:

$$\boldsymbol{d}_i^e = \left\langle d_x, d_y, d_z \right\rangle_i^{eT} \quad (i = 1,8) \tag{5}$$

$$\boldsymbol{r} = \left\langle \boldsymbol{c}_x, \boldsymbol{c}_y, \boldsymbol{c}_z \right\rangle^T \tag{6}$$

$$\boldsymbol{d}_i^e = \boldsymbol{r} \cdot (\boldsymbol{U}_i^e - \boldsymbol{U}_{i+8}^e) \quad (i = 1,8) \tag{7}$$

Finally, the local deformation at integration point level $\boldsymbol{u}$ are determined employing Serendipity shape functions [18] to approximate the three displacement fields over the element mid-plane. Thus the local relative displacement $\boldsymbol{u}$ evaluated for each integration point is:

$$\boldsymbol{u} = \left\langle u_x, u_y, u_z \right\rangle = \left\langle \sum_{i=1}^{8} N_i(\xi,\eta) d_{xi}, \quad \sum_{i=1}^{8} N_i(\xi,\eta) d_{yi}, \quad \sum_{i=1}^{8} N_i(\xi,\eta) d_{zi} \right\rangle, \tag{8}$$

where $\boldsymbol{N}_{i=1,8}$ are the Serendipity shape functions, (ξ, η) are the natural coordinates on the mid-plane of the element, and d_{xi}, d_{yi}, d_{zi} are the components of the local displacement vector at node i Eq. (5).

2.2. Resistance forces and tangent stiffness

Standard finite element techniques [18] are used to obtain the local nodal forces $\boldsymbol{f}^e$ and the local stiffness matrix $\boldsymbol{k}^e$ at element level. In particular, the three local stress component $\boldsymbol{\sigma}$ and stiffness $\boldsymbol{k}$ corresponding to the local displacement $\boldsymbol{u}$ (section 3.3.2) and (section 3.1) are integrated in the virtual work equation using Gaussian quadrature over the original interface area, leading to:

$$\boldsymbol{f}^e = \sum_{i=1}^{ng} \boldsymbol{N}_i^T \cdot \boldsymbol{\sigma}_i \cdot w(i) \cdot det\ j(i) \tag{9}$$

$$\boldsymbol{k}^e = \sum_{i=1}^{ng} \boldsymbol{N}_i^T \cdot \boldsymbol{k}_i \cdot \boldsymbol{N}_i \cdot w(i) \cdot det\ j(i) \tag{10}$$

with:

$$\boldsymbol{N}_i = \begin{bmatrix} N_1(\xi_i,\eta_i) & 0 & 0 & \ldots & N_8(\xi_i,\eta_i) & 0 & 0 \\ 0 & N_1(\xi_i,\eta_i) & 0 & \ldots & 0 & N_8(\xi_i,\eta_i) & 0 \\ 0 & 0 & N_1(\xi_i,\eta_i) & \ldots & 0 & 0 & N_8(\xi_i,\eta_i) \end{bmatrix}_{3\times 24} \tag{11}$$

where *ng* is the number of Gauss integration points, $w(i)$ is the weighting factor for the Gauss point i, $det\ j(i)$ is the determinant of the Jacobian for the transformation from the natural coordinates to the real local coordinates, $\boldsymbol{N}_{i=1,8}$ are the shape functions, and (ξ_i, η_i) are the natural coordinates over the mid-plane of the element.

The choice of an effective strategy for integrating local entities over the interface domain represents an important issue in the element formulation. In previous research [21], the results achieved using different procedures for the numerical integration in interface elements were compared. It was shown that the Newton-Cotes and Lobatto schemes with a reduced number of points (2x2) guarantees a smooth response, even in the case of high elastic stiffness, while the use of either higher number of points or Gauss quadrature leads to oscillations in the solution. Other studies [22] claimed the need of a high number of integration points in order to achieve accurate results because of the non-smooth profile of stresses in elements that are only partially damaged. In the analyses carried out in this research, the use of Gauss quadrature has always guaranteed smooth response and accurate results even increasing the number of integration points (section 4.1). This is due to the relatively low stiffness of mortar interfaces where cracks and damage mainly develop. As suggested in [21] other integration strategies could be more effective in the case of high interface stiffness.

The relations between local and global forces, $\boldsymbol{f}^e$ and $\boldsymbol{R}^e$ respectively, can also be defined considering the principle of virtual work leading to [20]:

$$\boldsymbol{R}_i^e = \boldsymbol{T}_{i,j}{}^T \boldsymbol{f}_j^e \qquad (i = 1,16 \text{ and } j = 1,8) \tag{12}$$

with:

$$\boldsymbol{R}_i^e = \langle R_X, R_Y, R_Z \rangle_i^T \quad \boldsymbol{f}_j^e = \langle f_x, f_y, f_z \rangle_j^T \ (i = 1,16 \text{ and } j = 1,8) \tag{13}$$

where $\boldsymbol{T}_{i,j}$ is a 3×3 transformation matrix representing first derivatives of local with respect to global displacement parameters:

$$\boldsymbol{T}_{i,j}=\frac{\partial \boldsymbol{d}_i^e}{\partial \boldsymbol{U}_j^e} \qquad \left(i=1,8;\ \ j=1,16\right) \tag{14}$$

$$\frac{\partial d_{n,i}^e}{\partial U_{m,j}^e}=\frac{1}{2}\left(\delta_{\mathrm{ij}}-\delta_{\mathrm{i(j-8)}}\right)\boldsymbol{r}_n\cdot\begin{Bmatrix}\delta_{1\mathrm{m}}\\ \delta_{2\mathrm{m}}\\ \delta_{3\mathrm{m}}\end{Bmatrix}+\frac{\partial \boldsymbol{r}_n}{\partial U_{m,j}^e}\cdot\left(\boldsymbol{U}_i^e-\boldsymbol{U}_{i+8}^e\right) \qquad \left(m \text{ and } n=1,3\right)$$

$$\frac{\partial \boldsymbol{r}_n}{\partial U_{m,j}^e}=\begin{bmatrix}\dfrac{\partial \boldsymbol{c}_x}{\partial U_{m,j}^e} & \dfrac{\partial \boldsymbol{c}_y}{\partial U_{m,j}^e} & \dfrac{\partial \boldsymbol{c}_z}{\partial U_{m,j}^e}\end{bmatrix}^T \qquad \left(j=1,16;\ \ m \text{ and } n=1,3\right) \tag{15}$$

$$\frac{\partial \boldsymbol{c}_x}{\partial U_{m,j}^e}=\frac{\boldsymbol{I}-\boldsymbol{c}_x\boldsymbol{c}_x{}^T}{\left|\boldsymbol{c}_{13}-\boldsymbol{c}_{24}\right|}\left[\frac{\left(\delta_{3j}-\delta_{1j}+\delta_{11j}-\delta_{9j}\right)}{2}\frac{\left(\boldsymbol{I}-\boldsymbol{c}_{13}\boldsymbol{c}_{13}{}^T\right)}{\left|\boldsymbol{v}_{24}\right|}-\frac{\left(\delta_{4j}-\delta_{2j}+\delta_{12j}-\delta_{10j}\right)}{2}\frac{\left(\boldsymbol{I}-\boldsymbol{c}_{13}\boldsymbol{c}_{13}{}^T\right)}{\left|\boldsymbol{v}_{24}\right|}\right]\begin{Bmatrix}\delta_{1m}\\ \delta_{2m}\\ \delta_{3m}\end{Bmatrix}$$

$\left(j=1,16;\ \ m=1,3\right)$

(16)

$$\frac{\partial \boldsymbol{c}_y}{\partial U_{m,j}^e}=\frac{I-\boldsymbol{c}_y\boldsymbol{c}_y{}^T}{\left|\boldsymbol{c}_{13}+\boldsymbol{c}_{24}\right|}\left[\frac{\left(\delta_{3j}-\delta_{1j}+\delta_{11j}-\delta_{9j}\right)}{2}\frac{\left(I-\boldsymbol{c}_{13}\boldsymbol{c}_{13}{}^T\right)}{\left|\boldsymbol{v}_{24}\right|}+\frac{\left(\delta_{4j}-\delta_{2j}+\delta_{12j}-\delta_{10j}\right)}{2}\frac{\left(I-\boldsymbol{c}_{13}\boldsymbol{c}_{13}{}^T\right)}{\left|\boldsymbol{v}_{24}\right|}\right]\begin{Bmatrix}\delta_{1m}\\ \delta_{2m}\\ \delta_{3m}\end{Bmatrix}$$

$\left(j=1,16;\ \ m=1,3\right)$

(17)

$$\frac{\partial \boldsymbol{c}_z}{\partial U_{m,j}^e}=\frac{\partial \boldsymbol{c}_x}{\partial U_{m,j}^e}\times\boldsymbol{c}_y+\boldsymbol{c}_x\times\frac{\partial \boldsymbol{c}_y}{\partial U_{m,j}^e} \qquad j=1,16;\ \ m=1,3 \tag{18}$$

where δ_{ij} is the Kronecker's delta: $\delta_{\mathrm{ij}}=\begin{cases}1 \text{ if i=j}\\ 0 \text{ if i}\neq\text{j}\end{cases}$.

Finally the global tangent stiffness $\boldsymbol{K}^e$, which represents the variation of the global forces with respect to global displacements, can be determined from Eq. (12). Applying the chain rule of differentiation $\boldsymbol{K}^e$ can be represented as a transformation of the local tangent stiffness matrix $\boldsymbol{k}^e$:

$$\boldsymbol{K}_{i,j}^{e} = \frac{\partial \boldsymbol{R}_{i}^{e}}{\partial \boldsymbol{U}_{j}^{e}} \qquad \left(i \text{ and } j = 1,16\right) \tag{19}$$

$$\boldsymbol{K}^{e} = \boldsymbol{T}^{T}\boldsymbol{k}^{e}\boldsymbol{T} + \sum_{i=1}^{8} \boldsymbol{f}_{i}^{e}\boldsymbol{G}_{i} \tag{20}$$

with

$$\boldsymbol{G}_{i,j,k} = \frac{\partial \boldsymbol{d}_{i}^{e}}{\partial \boldsymbol{U}_{j}^{e}\partial \boldsymbol{U}_{k}^{e}} . \tag{21}$$

The terms of $\boldsymbol{G}$, which are second derivatives of local with respect to global displacement parameters, can be obtained from first differentiation of $\boldsymbol{T}_{i,j}$ defined by Eq. (14) with respect to $\boldsymbol{U}^{e}$.

2.3. Multi-surface plasticity material model

The material nonlinearity that determines the behaviour of the 2D interface element in the proposed mesoscale model for brick-masonry is taken into account using the plasticity framework with a multi-surface plasticity criterion for mortar interfaces. Previously, non-smooth yield surfaces have been largely and successfully used in many engineering applications, from soil mechanic to metal plasticity [17]. With regard to brick-masonry, Lourenço and Rots [9] first and more recently Charimoon and Attard [23] used 1D nonlinear interface elements with a three-surface yield criterion to model failure in pure tension, compression, and shear.

In this work, the approach suggested by Carol *et al.* [6] and based on work-softening plasticity has been adopted, and the recent enhancements provided by Caballero *et al.* [24] for mesoscale analysis of quasi-brittle materials have also been considered. The formulation of Carol *et al.* is characterized by one hyperbolic yield function to simulate Mode I and Mode II fracture, providing smooth transition between pure tension and shear failure. A hyperbolic plastic potential different from the yield function is considered in order to avoid excessive

dilatancy and account for the actual roughness of the fracture surface. The model proposed in this work employs a second hyperbolic function, the cap in compression, to account for crushing in the mortar interfaces, which is obviously not required for interface elements representing cracks inside a brick.

The plasticity surface related to failure in tension and shear represent a direct description of Mode I and Mode II fracture in either mortar or brick interfaces. Initial cohesion, tensile strength and fracture energy can be determined directly from tests on single joint specimens. On the other hand, the cap in compression is not directly related to the actual physical behaviour of one of the brick-masonry components, but corresponds to a phenomenological representation of masonry resistance in compression. The strength in compression, considered as a cap material parameter, is different from the strength of mortar and brick-mortar interface and is assumed equal to the compressive strength of masonry. This last value can be determined in tests on small masonry specimens and corresponds to the compressive strength of confined mortar joint (i.e. mortar that cannot expand because of Poisson's effect). This was studied in previous research [25], where it was demonstrated that compressive forces on brick-masonry elements lead to triaxial compression in mortar and a compression and biaxial tension state in brick units, caused by the greater brick stiffness that prevents the mortar lateral expansion. Since the compressive strength of masonry depends not only on the material properties of brick and mortar but also on the inherent texture of masonry (i.e. geometrical proportion and spatial distribution of bricks and mortar), 3D failure criteria, coupled with the continuous approach, should be used for both mortar and bricks in order to capture actual stress distribution in the brick-masonry components under dominant compressive forces. As mentioned above, this would lead to an extremely high computational cost as well as to the need for solving numerical problems related to the localisation of the solution [11]. Notwithstanding, the proposed nonlinear interface element, associated only

with a plastic surface related to failure in tension and shear, could still be used in an alternative detailed mesoscale model for representing the physical brick-mortar interface and potential cracks in bricks. Using such a description, where both bricks and mortar layers would be modelled with 3D solid elements, the compressive failure of brick-masonry, characterized by the development of cracks in bricks along the direction of the compressive force, could be represented more accurately. However, such a detailed model would require a very large number of solid elements, especially for modelling strain/stress variations in mortar, thus posing potentially prohibitive computational demands for modelling the nonlinear response of real masonry panels. Therefore, while this alternative modelling approach is feasible with the proposed interface formulation, it is excluded from further consideration in this paper. It is also worth noting that even though the adopted phenomenological cap in compression for the nonlinear interface element is not directly related to actual behaviour of masonry components, it represents a good compromise between accuracy and computational efficiency in mesoscale compressive failure modelling of brick-masonry.

2.3.1. Variables, plastic surfaces and potentials

The local material model is formulated in terms of one normal and two tangential tractions $\boldsymbol{\sigma}$ Eq. (22) and relative displacements $\boldsymbol{u}$ (section 3.1) evaluated for each integration point over the reference mid-plane (Fig. 4).

$$\boldsymbol{\sigma} = \left\langle \tau_x, \tau_y, \sigma \right\rangle \tag{22}$$

In the case of mortar joints, the constitutive model for zero-thickness interfaces enables not only separations and damage to be evaluated, but it also accounts for the actual elastic deformations of mortar and brick-mortar interfaces. Specific elastic stiffness values, which

depend on the component elastic properties and dimensions of the joints, are considered assuming decoupling of the normal k_{n0} and tangential k_{t0} stiffness:

$$\boldsymbol{k_0} = \begin{bmatrix} k_{t0} & 0 & 0 \\ 0 & k_{t0} & 0 \\ 0 & 0 & k_{n0} \end{bmatrix} \tag{23}$$

If the masonry joints are not too thick the stiffness contributions k_{n0} and k_{t0} can be calculated as function of mortar joints geometry and mechanical properties, using the following expression:

$$k_{t0} = \frac{G_m}{h_j}; \quad k_{n0} = \frac{E_m}{h_j}, \tag{24}$$

where G_m and E_m are the shear and normal elastic modulus, respectively, and h_j is the thickness of the mortar joint. Otherwise k_{n0} and k_{t0} have also to account for the dimension and the material property of the bricks [9,26].

With regard to the brick interfaces the elastic stiffness corresponds to a penalty factor which should limit elastic deformations and prevent interpenetration in compression between the connected parts of each brick.

The elastic stiffness matrix $\boldsymbol{k}_0$ determines the interface behaviour in the elastic domain, before first cracks start developing, where the stress vector is proportional to relative displacements:

$$\boldsymbol{\sigma} = \boldsymbol{k}\boldsymbol{u} \quad \text{with} \quad \boldsymbol{k} = \boldsymbol{k}_0 \text{ and } \boldsymbol{u} = \boldsymbol{u}_{el} \tag{25}$$

The boundaries of elastic domain are marked by two smooth curves F_1 and F_2, corresponding to two hyperbolic surfaces each defined by three material variables (Fig. 5a):

$$F_1 = \tau_x^2 + \tau_y^2 - \left(C - \sigma \tan\phi\right)^2 + \left(C - \sigma_t \tan\phi\right)^2 = 0 \tag{26}$$

$$F_2 = \tau_x^2 + \tau_y^2 - \left(D + \sigma \tan\theta\right)^2 + \left(D - \sigma_c \tan\theta\right)^2 = 0 \tag{27}$$

F_1 represents the yield surface for Mode I and Mode II fracture, while F_2 is the cap in compression.

Both surfaces shrink with the development of plastic work (Fig. 5b), which is the work done by stresses and plastic deformations that drives the softening of the material parameters. The following evolution laws proposed by Caballero *et al.* [24] have been used:

$$A = A_0\left(1-\delta\right) \tag{28}$$

$$B = B_0 - \left(B_0 - B_r\right)\delta \tag{29}$$

with:

$$\delta = \begin{cases} \dfrac{1}{2}\left[1-\cos\left(\dfrac{\pi W_*}{G_*}\right)\right] & 0 \le W_* \le G_* \\ 1 & W_* > G_* \end{cases} \tag{30}$$

where A and B stand for the individual surface parameters of Eqs (26)-(27), as detailed in Table 1. The three material variables C, σ_t, $tan\phi$ associated with surface F_1 have explicit physical meaning as they represent the cohesion, the tensile strength and the friction angle at either mortar or brick interfaces. Their initial values C_0, σ_{t0}, $tan\phi_0$ as well as the residual value of the friction angle $tan\phi_r$ can be determined through experimental tests [26].

Regarding the parameters for the F_2 surface, on the other hand, the initial compressive strength σ_{c0} and its evolution can be directly established in tests on masonry specimens. Two internal plastic work variables, W_{pl1} and W_{pl2}, drive the degradation of the material variables and therefore the evolution of the plastic surfaces, F_1 and F_2, respectively:

$$dW_{pl1} = \begin{cases} \boldsymbol{\sigma} d\boldsymbol{u}_{pl1} & \sigma \ge 0 \\ \left(\sqrt{\tau_x^2 + \tau_x^2} + \sigma\, tan\,\phi\right)\sqrt{du_{x,pl1}^2 + du_{y,pl1}^2} & \sigma < 0 \end{cases} \tag{31}$$

$$dW_{pl2} = \boldsymbol{\sigma} d\boldsymbol{u}_{pl2} \tag{32}$$

W_{pl2} is the total plastic work done as the F_2 surface is traversed. Similarly, W_{pl1} is the plastic work performed as the F_1 surface is traversed, though the dissipation due to friction in the compressive range of σ is excluded [24].

The degradation of the material parameters, as expressed in Eqs (28)-(29)-(30), is also defined by the entity G_* which corresponds to either fracture energy or crushing energy as an intrinsic material property. Two different fracture energy values, $G_{f,I}$ for Mode I (tension) and $G_{f,II}$ for Mode II (shear), are considered for F_1 surface, such that the strength in tension and the cohesion vanish when W_{pl1} reaches $G_{f,I}$ and $G_{f,II}$, respectively, while a residual friction angle ϕ_r is considered for the behaviour in shear. In Figure 6a, typical traction-deformation curves are shown, where the dependence of the softening branch on the fracture energy for fracture Mode I can be clearly considered. In Figure 6b, the shear response is depicted for varying compressive normal stress (σ<0). When the plastic work reaches $G_{f,II}$, the residual shear strength becomes equal to the frictional component $\sigma \cdot tan\phi_r$. A crushing energy G_c is considered for F_2 surface in the model, which controls the shape of the softening curve for the compressive strength σ_c and for the two other material parameters D and $tan\theta$ given by Eqs (28)-(29)-(30) and Table 1.

A realistic treatment of dilatancy, which characterizes the behaviour of the frictional interface between bricks and mortar, is achieved by using a non-associated plastic flow for stress states on the F_1 surface. Similar to the work of Carol *at el.* [6], a hyperbolic plastic potential function Q_1, different from the plastic surface F_1, is assumed, and this determines the plastic/cracking deformation components $\boldsymbol{u}_{pl1}$:

$$Q_1 = \tau_x^2 + \tau_y^2 - \left(C_Q - \sigma \tan\phi_Q\right)^2 + \left(C_Q - \sigma_t \tan\phi_Q\right)^2 = 0 \tag{33}$$

where $tan\phi_Q$ and C_Q, along with the tensile strength σ_t, define the shape of the hyperbola for plastic potential Q_1. The two parameters, $tan\phi_Q$ and C_Q, reduce when the plastic work variable W_{pl1} increases, in accordance with the same evolution laws defined for the friction angle $tan\phi$ and cohesion C (Eqs. (28)-(29), Table 1). The evolution of the plastic potential

reflects the intrinsic features of dilatancy in granular material, which reduces when shear sliding increases and is very limited in the case of high compressive stresses.

On the other hand, associated plastic flow is considered for stress states on the F_2 surface:

$$Q_2 = F_2 \tag{34}$$

2.3.2. Solution of the plasticity problem

The two plastic surfaces F_1 and F_2 intersect non-smoothly at singularity points, thus requiring the solution of a multi-surface plasticity problem [17] for determining the stress vector $\boldsymbol{\sigma}$, consistent stiffness $\boldsymbol{k}$ and internal plastic work variables $W_{pl1}$and W_{pl2}.

The increment of local deformations $d\boldsymbol{u}_n$ is the primary variable which is constant in the local iterative procedure, and this is taken as the difference between local nodal displacements at time n and time n-1, as obtained from Eq. (8). In this context, the solution at current time step n refers to a generic global iteration, while the quantities at previous time step n-1 are those at global convergence.

The trial elastic stress vector can be calculated using the elastic stiffness matrix $\boldsymbol{k}_0$:

$$\boldsymbol{\sigma}_{n,trial} = \boldsymbol{\sigma}_{n-1} + \boldsymbol{k}_0 d\boldsymbol{u}_n \tag{35}$$

When such stresses cross one or both plastic surfaces, the solution for the plasticity problem is obtained through the backward Euler method assuming the Kuhn-Tucker complementarity conditions and Koiter's flow rules [17]. The increment of total strain can be divided into two components, the elastic and the plastic part, the latter consisting of two contributions associated with either of the plastic potential surfaces:

$$d\boldsymbol{u} = d\boldsymbol{u}_{el} + d\boldsymbol{u}_{pl1} + d\boldsymbol{u}_{pl2} \tag{36}$$

with

$$d\boldsymbol{u}_{pl1} = d\lambda_1 \frac{\partial Q_1}{\partial \boldsymbol{\sigma}} \tag{37}$$

$$d\boldsymbol{u}_{pl2} = d\lambda_2 \frac{\partial Q_2}{\partial \boldsymbol{\sigma}} \tag{38}$$

where $d\lambda_1$ and $d\lambda_2$ are the increments of the plastic multipliers for the F_1 and F_2 surfaces, respectively.

The solution is obtained by considering the loading/unloading conditions [17]:

$$d\lambda_i \geq 0; \quad F_i\left(\boldsymbol{\sigma}, W_{pli}\right) \leq 0; \quad d\lambda_i F_i\left(\boldsymbol{\sigma}, W_{pli}\right) = 0 \quad \text{with} \quad \text{i=1,2} \tag{39}$$

The procedure used by Caballero *et al.* [24] for smooth plasticity criteria has been employed and extended to the case of multi-surface plasticity. The plastic multiplier calculation is integrated with the fracture work and the incremental traction-deformation computation. A local Newton-Raphson strategy is employed, where the local system of nonlinear equations is solved using a monolithic iteration technique with sub-stepping. The procedure is based on an elastic predictor and on a corrector stress based on fracture energy.

Three different cases can occur as shown in Figure 7: the trial stress vector can cross either F_1, F_2 or both surfaces. In the following, the procedure employed for the last case, which is the most general, is detailed.

The stress vector, plastic work variables and plastic multipliers can be determined by solving the nonlinear system of equations in residual form:

$$\begin{cases} \boldsymbol{R}_{\boldsymbol{\sigma},n} = \boldsymbol{\sigma}_n - \boldsymbol{\sigma}_{n-1} - \boldsymbol{k}_0 \left(d\boldsymbol{u}_n - d\lambda_{1,n} \left.\dfrac{\partial Q_1}{\partial \boldsymbol{\sigma}}\right|_n - d\lambda_{2,n} \left.\dfrac{\partial Q_2}{\partial \boldsymbol{\sigma}}\right|_n \right) = 0 \\ R_{W_{pl1,n}} = W_{pl1,n} - dW_{pl1,n}\left(\boldsymbol{\sigma}, W_{pl1,n}, d\lambda_{1,n}\right) - W_{pl1,n-1} = 0 \\ R_{W_{pl2,n}} = W_{pl2,n} - dW_{pl2,n}\left(\boldsymbol{\sigma}, W_{pl2,n}, d\lambda_{2,n}\right) - W_{pl2,n-1} = 0 \\ R_{F_1,n,i} = F_1\left(\boldsymbol{\sigma}_n, W_{pl1,n}\right) = 0 \\ R_{F_1,n,i} = F_2\left(\boldsymbol{\sigma}_n, W_{pl2,n}\right) = 0 \end{cases} \tag{40}$$

where $\boldsymbol{\sigma}_{n-1}$ and $W_{pl1,n-1}$ $W_{pl2,n-1}$ are the stresses and plastic work variables at convergence in the previous time (pseudo-time) step, $dW_{pl1,n}$ and $dW_{pl2,n}$ are the increments of plastic work variables for the current step n, and $\boldsymbol{\sigma}_n$, $W_{pl1,n}$, $W_{pl2,n}$ $\lambda_{l1,n}$ and $\lambda_{l2,n}$ are the unknowns to be

determined. According to the full Netwon-Raphson procedure, the system in Eq. (40) is linearised leading to:

$$\boldsymbol{R}_{n,i+1} \cong \boldsymbol{R}_{n,i} + \left[\boldsymbol{J}\right]_{n,i} \left\langle d\boldsymbol{\sigma} \quad dW_{pl1} \quad dW_{pl2} \quad d\lambda_1 \quad d\lambda_2 \right\rangle_{n,i}^{T} = 0 \tag{41}$$

thus:

$$\left\langle d\boldsymbol{\sigma} \quad dW_{pl1} \quad dW_{pl2} \quad d\lambda_1 \quad d\lambda_2 \right\rangle_{n,i}^{T} = -\left[\boldsymbol{J}\right]_{n,i}^{-1} \boldsymbol{R}_{n,i} \tag{42}$$

where:

$$\boldsymbol{R}_{n,i} = \left\langle \boldsymbol{R}_{\boldsymbol{\sigma}} \quad R_{W_{pl1}} \quad R_{dW_{pl2}} \quad R_{d\lambda_1} \quad R_{d\lambda_2} \right\rangle_{n,i}^{T} \tag{43}$$

$$\left[\boldsymbol{J}\right]_{n,i} = \left[\begin{array}{c|c|c|c|c} \boldsymbol{I}_3 + \boldsymbol{k}_0 d\lambda_1 \dfrac{\partial^2 Q_1}{\partial \boldsymbol{\sigma}^2} + \boldsymbol{k}_0 d\lambda_2 \dfrac{\partial^2 Q_2}{\partial \boldsymbol{\sigma}^2} & \boldsymbol{k}_0 d\lambda_1 \dfrac{\partial^2 Q_1}{\partial \boldsymbol{\sigma} \partial W_{pl1}} & \boldsymbol{k}_0 d\lambda_2 \dfrac{\partial^2 Q_2}{\partial \boldsymbol{\sigma} \partial W_{pl2}} & \boldsymbol{k}_0 \dfrac{\partial Q_1}{\partial \boldsymbol{\sigma}} & \boldsymbol{k}_0 \dfrac{\partial Q_2}{\partial \boldsymbol{\sigma}} \\ \hline -\dfrac{\partial dW_{pl1}}{\partial \boldsymbol{\sigma}} & 1 - \dfrac{\partial dW_{pl1}}{\partial W_{pl1}} & 0 & -\dfrac{\partial dW_{pl1}}{\partial \lambda_1} & 0 \\ \hline -\dfrac{\partial dW_{pl2}}{\partial \boldsymbol{\sigma}} & 0 & 1 - \dfrac{\partial dW_{pl2}}{\partial W_{pl2}} & 0 & -\dfrac{\partial dW_{pl2}}{\partial \lambda_2} \\ \hline \dfrac{\partial F_1}{\partial \boldsymbol{\sigma}} & \dfrac{\partial F_1}{\partial W_{pl1}} & 0 & 0 & 0 \\ \hline \dfrac{\partial F_2}{\partial \boldsymbol{\sigma}} & 0 & \dfrac{\partial F_1}{\partial W_{pl1}} & 0 & 0 \end{array}\right]_{n,i} \tag{44}$$

in which $\boldsymbol{I}_3$ represents the 3 by 3 identity matrix in the stress space.

The local solution at time step n for global iteration k can be found simply by iterative correction of the variables until convergence, as defined in terms of the norm of the residuals being less than a tolerance δ:

$$\left\{\begin{array}{c} \boldsymbol{\sigma} \\ W_{pl1} \\ W_{pl2} \\ \lambda_1 \\ \lambda_2 \end{array}\right\}_{n} = \left\{\begin{array}{c} \boldsymbol{\sigma} \\ W_{pl1} \\ W_{pl2} \\ \lambda_1 \\ \lambda_2 \end{array}\right\}_{n-1} + \sum_{j} \left\{\begin{array}{c} d\boldsymbol{\sigma} \\ dW_{pl1} \\ dW_{pl2} \\ d\lambda_1 \\ d\lambda_2 \end{array}\right\}_{n,j} \qquad \text{with } j \text{ increased until } \sqrt{\boldsymbol{R}_{n,i} \boldsymbol{R}_{n,i}} \le \delta \tag{45}$$

At the end of the iterative process, the local tangent stiffness $\boldsymbol{k}_n$, consistent with the numerical solution procedure, is obtained as the first derivative of the stresses with respect to the strains:

$$\boldsymbol{k}_n = \left(\frac{\partial \boldsymbol{\sigma}}{\partial \boldsymbol{u}} \right)_n \tag{46}$$

This can be determined by linearising the nonlinear equations for the stress components, included in $\boldsymbol{R}_{\sigma,n}$, whereby the Jacobian $\boldsymbol{J}_{\mathrm{n}}$, obtained at convergence for the current global iteration, is employed to determine $\boldsymbol{k}_{\mathrm{n}}$ [27]:

$$\boldsymbol{k}_n = \boldsymbol{P}^T \boldsymbol{J}_n^{-1} \boldsymbol{P} \boldsymbol{k}_0 \tag{47}$$

where $\boldsymbol{P}$ corresponds to the projection matrix on the stress space: $\boldsymbol{P} = \left[\boldsymbol{I}_3 \quad \boldsymbol{0}_{3\times 4} \right]^T$, $\boldsymbol{I}_3$ is a 3×3 identity matrix, and $\boldsymbol{0}_{3\times 4}$ is a 3×4 null matrix.

To enhance the robustness of the local solution procedure, a substepping strategy is employed so that a solution can be found even for relatively large increments of local strains $d\boldsymbol{u}_n$. When the number of iterations required to solve Eq. (40) is greater than a prescribed value n_{max1}, the substepping procedure is activated and the total increment of local strains $d\boldsymbol{u}_{\mathrm{n}}$, as determined from the increment of global displacements, is divided into m local substeps [27]:

$$d\boldsymbol{u}_{n,k} = \alpha_k \, d\boldsymbol{u}_n \qquad \text{with } \sum_{k=1}^{m} \alpha_k = 1 \text{ and } 0 < \alpha_k \leq 1 \quad \text{k=1..m} \tag{48}$$

An adaptive multi-level substepping strategy is employed, where the step reduction coefficient α_k depends on a prescribed constant factor $\gamma > 1$ and on the substepping level n according to $\alpha_k = 1/\gamma^n$. When the number of iterations required for a substep k at level n is greater than n_{max1}, the level is increased and the reduction coefficient is reduced to $\alpha_k = 1/\gamma^{n+1}$. Conversely, if the local solution is successfully found for γ consecutive substeps, the substep level is reduced and the reduction coefficient for the following substep is increased to $\alpha_{k+1} = 1/\gamma^{n-1}$. The procedure stops when $\sum_{k=1}^{m} \alpha_k = 1$ or when the total number of

local iterations, the sum of the iterations required at each substep, is greater than a prescribed maximum value n_{max2}. In the former case, the local solution for the total increment of local strains $d\boldsymbol{u}_{\mathrm{n}}$, is determined, while in the latter case, step reduction at the global structural level may be required. As far as the local solution is concerned, at each substep the trial elastic stress is first obtained, and the activation of either or both plastic surfaces is subsequently checked, as in the case of monolithic calculation without substeps. If at substep k a plastic surface is crossed and the solution is found, in the following steps the solution is sought either along the same surface or at singularity points, where the two surfaces intersect each other.

At each substep k the stress vector, the plastic work variables and plastic multipliers are solved for using Eq. (40), where $d\boldsymbol{u}_n$ is substituted by $d\boldsymbol{u}_{n,k}$, and then transferred to the next step, until a solution is obtained for the last substep which corresponds to the full increment $d\boldsymbol{u}_n$. Finally, the consistent stiffness matrix is determined by adding the different contributions from each substep, following the approach proposed in [24] aimed at preserving quadratic convergence. This process involves differentiating the equations in (40), written for a substep k, with respect to $d\boldsymbol{u}_n$:

$$\frac{\partial}{\partial \boldsymbol{u}_n}\begin{bmatrix} \boldsymbol{\sigma}_{n\text{-}1+k/m}+\boldsymbol{k_0}\left(d\lambda_{1,n-1+k/m}\dfrac{\partial Q_1}{\partial \boldsymbol{\sigma}}_{n+k/m}+d\lambda_{2,n-1+k/m}\dfrac{\partial Q_2}{\partial \boldsymbol{\sigma}}_{n-1+k/m}\right) \\ W_{pl1,n-1+k/m}-dW_{pl1,n-1+k/m}\left(\boldsymbol{\sigma},W_{pl1,n-1+k/m},d\lambda_{1,n-1+k/m}\right) \\ W_{pl2,n-1+k/m}-dW_{pl2,n-1+k/m}\left(\boldsymbol{\sigma},W_{pl2,n-1+k/m},d\lambda_{2,n-1+k/m}\right) \\ F_1\left(\boldsymbol{\sigma}_{n-1+k/m},W_{pl1,n-1+k/m}\right) \\ F_2\left(\boldsymbol{\sigma}_{n-1+k/m},W_{pl2,n-1+k/m}\right) \end{bmatrix} = \frac{\partial}{\partial \boldsymbol{u}_n}\begin{bmatrix} \boldsymbol{\sigma}_{n-1+(k-1)/m}+\boldsymbol{k_0}d\boldsymbol{u}_{n,k} \\ W_{pl1,n-1+(k-1)/m} \\ W_{pl2,n-1+(k-1)/m} \\ 0 \\ 0 \end{bmatrix} \quad (49)$$

At the first substep k=1, $\dfrac{\partial \sigma_{n-1}}{\partial \boldsymbol{u}_n}=0$, $\dfrac{\partial W_{pl1,n-1}}{\partial \boldsymbol{u}_n}=0$, $\dfrac{\partial W_{pl2,n-1}}{\partial \boldsymbol{u}_n}=0$ and the stiffness matrix can be determined using Eq. (47) applying the chain rule of differentiation:

$$\frac{\partial \boldsymbol{\sigma}_{n\text{-}1+1/m}}{\partial \boldsymbol{u}_n}=\frac{\partial \boldsymbol{\sigma}_{n\text{-}1+1/m}}{\partial \boldsymbol{u}_{n-1+1/m}}\frac{\partial \boldsymbol{u}_{n-1+1/m}}{\partial \boldsymbol{u}_n}=\alpha_1 \boldsymbol{P}^T \boldsymbol{J}_{n-1+1/m}^{-1}\boldsymbol{P}\boldsymbol{k}_0 \,. \quad (50)$$

For a subsequent generic subincrement $2 \le k \le m$ the contribution from the previous substeps has to be taken into account [24] leading to:

$$\frac{\partial \sigma_{n\text{-}1+k/m}}{\partial \boldsymbol{u}_n} = \boldsymbol{P}^T \boldsymbol{J}^{-1}_{n-1+k/m} \begin{bmatrix} \dfrac{\partial \sigma_{n\text{-}1+(k-1)/m}}{\partial \boldsymbol{u}_n} + \alpha_k \boldsymbol{k}_0 \\ \dfrac{\partial W_{pl1,n\text{-}1+(k-1)/m}}{\partial \boldsymbol{u}_n} \\ \dfrac{\partial W_{pl2,n\text{-}1+(k-1)/m}}{\partial \boldsymbol{u}_n} \\ \boldsymbol{0}_{2,3} \end{bmatrix} \tag{51}$$

where the consistent stiffness matrix $\boldsymbol{k}_n$ is obtained from Eq. (50) as the final matrix corresponding to $k=m$.

In the analyses carried out employing the proposed mesoscale model with nonlinear interfaces, the use of substepping is found particularly effective when cracks develop along brick interfaces, principally due to the high elastic stiffness which lead to trial stresses that are relatively far from the plastic surfaces.

3. Numerical Examples

The proposed nonlinear interface element has been implemented in ADAPTIC [28], a general finite element code for nonlinear analysis of structures under extreme static and dynamic loading, which is used here to demonstrate the accuracy and effectiveness of proposed mesoscale modelling approach for brick-masonry. Numerical results are compared hereafter with outcomes of experimental tests on URM panels, where both the in-plane and out-of-plane responses of URM elements are investigated.

3.1. In-Plane Response

Some of the results obtained by Vermeltfoort & Raijmakers [29] in shear tests on single-leaf panels are considered here for experimental-numerical comparisons. Two solid brick-

masonry walls are analysed, which correspond to the identical wall specimens J4D and J5D and to specimen J7D in [29].

In the tests, all the walls were first preloaded with a vertical top pressure, p_v=0.3 MPa for J4D and J5D and p_v=2.12 MPa for J7D, and a horizontal load F_h was then applied in the plane of the walls at the top edge under displacement control up to collapse (Fig. 8a). The three URM panels have a width-height ratio of around 1 (990×1000 mm^2), and they all feature 18 brick layers of which only 16 were loaded, and the remaining 2 were fixed to steel beams so as to keep the top and bottom edges of the element straight during the test. Each brick unit is 204×98×50 mm^3, while the bed and head mortar joints are 12.5 mm thick.

During the tests, some horizontal cracks first appeared at the top and bottom of the walls, and then cracks started developing diagonally, along the bed and head mortar joints and through the bricks, up to failure. The experimental response was characterized by a softening branch which started when diagonal cracks suddenly appeared in the centre of the specimens.

The walls are modelled here using the mesoscale approach detailed in previous sections. Numerical problems occurred when performing static analyses with standard displacement control techniques [16] especially for the case of higher normal pressure, which were caused by a sudden release of elastic energy in bulk material when cracks spread along interfaces. In order to determine the solution up to collapse, a dynamic analysis procedure is utilised, allowing the sudden release of elastic energy to be balanced by kinetic and viscous energy. In all analyses, a fixed value of velocity v=0.1 mm/s is applied at all the nodes at the top of the wall. Moreover prescribed vertical displacements are applied at the same nodes to reproduce the effect of the vertical pressure p_v, and all the displacements at the bottom are fully restrained to represent a fixed support. Finally, zero acceleration is assigned to the top nodes during the analysis to ensure a linear variation with time of the top wall displacements.

Tables 2 and 3 show the mechanical properties for brick and brick-mortar interfaces employed in the analyses. These values, mainly determined from tests on single masonry components (units and mortar), were reported in previous research [9,23,26]. Moreover, regarding the clay bricks, an elastic modulus E_b=16700 MPa and a Poisson ratio ν_b=0.15 are assumed [9,26], while a density $\rho_b=19\cdot10^{-9}$ Ns^2/mm^4 and mass-proportional damping, corresponding to a damping ratio ζ=5%, are used for the solid elements to represent inertia and damping effects.

In order to evaluate the performance of the proposed mesoscale model for brick-masonry, the results obtained from different meshes have been compared. In 3D nonlinear models, the use of a fine mesh could become prohibitively expensive; therefore, the choice of the coarsest possible mesh that achieves acceptable accuracy is fundamental in order to reduce the computational effort in detailed modelling of URM structures. Two different meshes have been considered and compared in the analyses, as shown in Figure 8b. For the coarser mesh (mesh 1), only one 20-noded solid element is used per half brick, such that two interface elements are employed for each bed joints with only one interface element for each head joint and for modelling potential vertical cracks at the mid-plane of the bricks (brick-brick interface). In the finer mesh (mesh 2), each half unit is modelled using four solid elements, thus corresponding to a refinement of mesh 1 where the number of elements along the x and z directions is doubled. Therefore, four interfaces are used for each bed joint, and two interfaces are employed for each head joint and at the mid-plane of each brick unit.

The influence of the number of Gauss points in the nonlinear interface has also been investigated, so as to establish whether increasing the number of integration points leads to improved solution accuracy as a substitute for mesh refinement. Figure 9 provides experimental-numerical comparisons, where the experimental load-displacement curves for J4D, J5D and J7D walls are compared with the numerical results determined using the

coarser mesh (mesh 1) and 7x7 Gauss points for integration over the interface elements. In this figure, the numerical predictions reported by Lourenço & Rots [9] and calculated using planar elements (4×2 8-noded 2D elements for each brick) and nonlinear line interfaces are also shown. A good agreement between experimental and numerical results can be observed up to collapse, including initial stiffness, maximum capacity and the post-peak response of the walls. The predicted response is smooth for walls J4D and J5D subject to the lower vertical load p_v, while it exhibits jumps in the steep softening branch for wall J7D. The predictions of the proposed modelling approach are generally close to those reported in [9] for all walls, with the current predictions of the post-peak response for wall J7D evidently better.

Figure 10 depicts the influence of both mesh refinement and the number of Gauss points used for the interface elements. The results obtained using mesh 1 and mesh 2 are compared, where two different curves are shown for the coarser mesh, obtained respectively using 3×3 and 7×7 Gauss points, while only 3×3 Gauss point are employed for mesh 2. The predictions of mesh 1 with the larger number of integration points are coincident with those of mesh 2, while the predictions of mesh1 with 3×3 Gauss points exhibit some minor discrepancies in comparison. These outcomes show that the use of an increased number of integration points (super-integration) for interface elements provides smooth and accurate results, very close to those achieved through mesh refinement. This is particularly important since integration refinement is much less computationally demanding than mesh refinement.

The employment of super-integration for the interface is particularly effective since the 3D solid elements, representing bricks, generally have a much higher stiffness than damage interfaces. Therefore, these 3D elements behave as rigid blocks, thus the change in the interface displacement field upon mesh refinement is negligible.

Finally, Figure 11 shows the deformed shape, and the interface plastic work contours at collapse, which are compared to the crack paths surveyed in the tests for walls J4D and J5D. The results shown are those from mesh 1 with 7×7 Gauss points, where the plastic work W_{pl1} associated with the F_1 plastic surface assumes maximum values close to the fracture energies $G_{f,II}$ along the diagonal direction of the wall, while plastic work W_{pl2} associated with F_2 assumes high values close to the crushing energy G_c in the compressed bed joints at the two edges of the wall. These predictions are in good agreement with the main crack paths and with the results reported in [9].

3.2. Out-of-plane response

Numerical analyses are also carried out to establish the effectiveness of the developed mesoscale modelling approach for investigating the out-of-plane behaviour of URM walls, where comparisons are made against the experiments performed by Bean Popehn *et al.* [30] and Chee Liang [31].

Bean Popehn *et al.* [30] carried out experiments to investigate the buckling behaviour of slender URM walls subject to vertical and out-of-plane lateral loads. The static response of a clay brick-masonry panel 3.26 m high and 0.803 m wide with a thickness of 89.9 mm (specimen B1-25 in [30]) is considered here, where the brick units are 89.9×57.2×193.7 mm^3 and the joints are 10 mm thick. The wall, supported against out-of-plane displacements at the two horizontal edges, is firstly loaded by a vertical force P_v=111 kN, which is followed by an out-of-plane horizontal force F_h using a whittletree arrangement with spreader beams that allowed a close representation of a uniform load distribution. The lateral supports did not represent perfect simple supports, thus providing some resistance to the wall rotation. Accoridngly, an effective height of the wall was established as 2.41 m, measuring the distance between the two points of inflection. In the test, the wall exhibited linear behaviour

until some horizontal cracks occurred in the bed joints around mid-height, then increasing the lateral load, a single large horizontal crack developed when the maximum wall capacity was reached. The test continued under displacement control in order to assess the post-peak behaviour.

While mechanical properties for the components (units, mortar) were not reported [30], some average properties for masonry assumed as a continuum material (i.e. flexural tensile strength σ_{mt}=0.372 MPa) were provided. In previous research [12], it was shown that the collapse mechanism of walls loaded out-of-plane is different from that of URM elements loaded in-plane, because it is determined mainly by the tensile instead of the shear response. Therefore, the tensile strength σ_{t0} and the Mode-I fracture energy $G_{f;I}$ for mortar joints are the key parameters in advanced mesoscale models for studying the out-of-plane capacity and the post-peak response of URM walls.

As suggested in [12], σ_{t0} can be calculated from σ_{mt}, which is obtained in physical tests on the assumption of an elastic response, considering a uniform plastic distribution of tensile stresses over the interface and fixing the centre of rotation at the external edge of the masonry panel cross section. Thus the simple relation $\sigma_{t0}=1/3\cdot\sigma_{mt}$ has been employed in the current analyses. Moreover, in assessing the behaviour of slender walls under vertical loads when flexural buckling is a potential cause of failure, other fundamental parameters to be accurately determined are the elastic modulus of bricks and mortar joints. Since these values were also not reported [30], the elastic stiffness for brick and mortar has been calibrated so as to allow good correlation against the initial wall stiffness as observed in the tests.

Table 4 provides the mechanical properties used for the nonlinear interfaces, while an elastic modulus E_b=10000 MPa and a Poisson ratio ν_b=0.15 are assumed for bricks. In the performed analyses, according to the description of the test setup and the observed experimental behaviour [30], the initial load P_v is applied considering an eccentricity equal to 7 mm to

represent initial imperfections, while a uniform distribution of nodal forces is used to represent the variable out-of-plane horizontal loads.

The wall has been represented as a simply supported structure, considering the effective height and using the coarsest mesh allowable in the proposed modelling approach, utilising only one solid element for half a unit. Different numbers of Gauss points are also considered to establish whether increasing the number of integration points leads to improved accuracy as in the analysis of walls loaded in-plane. All the predictions are obtained using static analysis with standard arc-length displacement control [16].

Figure 12 compares the experimental load deflection response with that predicted using 3×3, 7×7 and 10×10 Gauss points for interface elements. The results achieved confirm the effectiveness of using a high number of integration points, which provide smooth and accurate results. More importantly, a comparison is made in Figure 12 between the predictions accounting for and neglecting geometric nonlinearity, including large displacements. These results demonstrate the importance of accounting for geometric nonlinearity in the mesoscale model for masonry, as it clearly enables a more accurate prediction of the actual behaviour of slender walls. Neglecting geometric nonlinearity leads to a significant inaccuracy for walls loaded by vertical and horizontal actions, where the strength is typically determined by out-of-plane instability. Furthermore, the consideration of geometric nonlinearity is essential for modelling the buckling response of masonry panels under vertical loading. As shown in Figure 13, which depicts the buckling response under vertical load P_v for wall B1-25 are shown, the consideration of geometric nonlinearity assuming linear material behaviour enables the elastic buckling load to be obtained. Obviously, a purely linear wall response would be obtained for the same case ignoring geometric nonlinearity. Furthermore, the same figure shows the added influence of material

nonlinearity for the considered wall, which is shown in this case to affect only the post-peak behaviour.

In the final comparison, the out-of-plane behaviour of a solid wall, simply supported along its four edges and subjected to bi-axial bending, is considered, where reference is made to experiments undertaken by Chee Liang [31] on two identical specimens wall 8 and wall 12. The single-leaf URM panel is 1190 mm high, 795 mm wide and 53 mm thick, comprising 112x53x36 mm^3 bricks and 10 mm thick mortar joints. The two specimens were loaded up to collapse by applying a uniform out-of-plane pressure through an air-bag sandwiched between the wall and a stiff reacting frame. Another stiff steel frame was connected to wall on the other side, so as to prevent out-of-plane displacements and provide fixed supports along the four edges. Tests were also performed on components, where the compressive strength of mortar, the tensile and compressive strength of bricks and the flexural strength of masonry were determined. As mentioned above, the out-of-plane capacity of the wall is strongly influenced by the tensile strength of the masonry joints, and its actual initial stiffness is affected by both the brick and mortar elastic modulus. These values were not determined experimentally [31]; therefore, the same procedure described before for relating the mortar tensile strength to the masonry flexural resistance is used. Table 5 provides the material parameters used for the interfaces elements, which correspond to the values used in [12] for the same wall, while the elastic stiffness of brick and mortar are assumed the same as in [13]. Figure 14 provides the numerical-experimental comparisons, where one 20-noded solid element is used for each half brick and 3×3 Gauss points for each interface element. The experimental results reported in [31] for wall 8 and wall 12 correspond to a partial load-displacement curve for wall 8 and the maximum capacity for both walls, where the displacement δ in the figure is at the centre of the wall. Good agreement can be observed between the numerical and experimental results. Using the material parameters for the

interfaces as suggested in [12], a maximum lateral pressure for the wall, very close to the experimental capacity and to the collapse pressure determined in [12] through a 3D limit analysis approach, is established. Unlike limit analysis, however, the proposed modelling approach enables the prediction of the initial stiffness and the post-peak response of the wall loaded out-of-plane. Finally, Figure 15 shows the deformed shape at collapse, which is compared with the actual crack pattern. The large vertical crack which runs along the head mortar joints and bricks as well as the continuous diagonal cracks observed in the tests are well represented using the proposed mesoscale model with nonlinear interface elements.

4. **Conclusion**

This paper presents a nonlinear interface element which is incorporated into a mesoscale model for nonlinear analysis of URM structures. The proposed mesoscale approach considers a detailed description for the 3D arrangement that characterises the texture of walls in URM buildings. Compared to previous mesoscale models for brick-masonry, the proposed approach accounts for both geometric and material nonlinearity and is based on the use of 2D nonlinear interface elements along with 3D solid elements, allowing the simulation of both the in-plane and out-of-plane response of URM walls.

A co-rotational formulation is adopted to account for geometric nonlinearity, including large displacement effects, and a work-softening non-associated plasticity approach, utilising a multi-surface plasticity criterion, is employed for the force-displacement material law at the interfaces.

The results of numerical analyses carried out to investigate both the in-plane and the out-of-plane response of brick-masonry panels up to collapse are presented, where comparisons are made against experimental outcomes. It is shown that the use of the proposed nonlinear 2D interface elements with 3D brick elements allows the consideration of both initial and

damage-induced anisotropy of brick-masonry. The main features of the structural behaviour, including initial stiffness, maximum capacity and post-peak response, are also accurately determined. In performing numerical simulations, the mesh density and the number of Gauss points for the interface elements are varied so as to establish the coarsest mesh that can still achieve reasonable accuracy in detailed nonlinear analysis of URM structures. It is shown that the use of only one 20-noded 3D element per half brick with the associated 2D interface elements provides good accuracy for both in-plane and out-of-plane nonlinear analysis, and that increasing the number of Gauss points can substitute for mesh refinement in achieving improved accuracy.

The results achieved demonstrate the significant potential of the proposed approach. The detailed mesoscale model with nonlinear interfaces, while potentially associated with significant computational demands, can be incorporated into a full multiscale approach in which the accurate mesoscale description and the structural scale are fully coupled, thus allowing the nonlinear analysis of larger scale structures [14]. This is an area of research that is currently being pursued by the authors.

Acknowledgement

The authors gratefully acknowledge the support provided for this research by the 7th European Community Framework Programme through a Marie Curie Intra-European Fellowship (Grant Agreement Number: PIEF-GA-2008-220336).

References

1. Goodman RE, Taylor RL, Brekke T. A model for the mechanics of jointed rock, J. Soil Mech. Found. Div. Proc. ASCE 1968; **94**, SM 3:637-659.

2. Rots JG. Computational modeling of concrete structures, PhD Thesis, Delft University of Technology, 1988.
3. Alfano G, Crisfield MA. Finite element interface models for delamination analysis of laminated composites: mechanical and computational issues, Int. J. Numer. Methods Engrg 2001; **50**:1701-1736.
4. Seguarado J, LLorca J. A new three-dimensional interface finite element to simulate fracture in composites, Int. J Solids and Struct. 2004; **41**:2977-2993.
5. Brocks W, Cornec A, Scheider I. Computational Aspects of Nonlinear Fracture Mechanics; In: I. Milne, R. O. Ritchie, B. Karihaloo (Eds.): Comprehensive Structural Integrity - Numerical and Computational Methods 2003. Vol. 3, Oxford: Elsevier, 127-209.
6. Carol I, Lopez CM, Roa O. Micromechanical analysis of quasi-brittle materials using fracture-based interface elements, Int. J. Numer. Methods Engrg 2001; **52**:193-215.
7. Alfano G, Sacco E. Combining interface damage and friction in cohesive-zone model, Int. J. Numer. Methods Engrg 2006; **68**:542-582.
8. Dhanasekar M, Page AW, Kleeman PW. The failure of brick masonry under biaxial stresses, Proc. Instn. Civ. Eng. 1985; **79**, 2: 295-313.
9. Lourenço PB, Rots JG. Multisurface Interface Model for Analysis of Masonry Structures, . J. Engrg. Mech. ASCE 1997; **123**, 7:660-668.
10. Gambarotta L, Lagomarsino S. Damage models for the seismic response of brick masonry shear walls. Part I: the mortar joint model and its applications, Earthquake Eng. Struct. Dynam. 1997; **26**:423-439.
11. Shien-Beygi B, Pietruszczak S. Numerical analysis of structural masonry: mesoscale approach, Computer and Struct. 2008; **86**:1958-1973.

12. Milani G. 3D upper bond limit analysis of multi-leaf masonry walls, Int. J. Mechanical Sciences 2008; **50**:817-836.
13. Griffith MC, Lam NTK., Wilson JL, Doherty K. Experimental investigation of unreinforced brick masonry walls in flexure, J. Struct. Engrg. ASCE 2004; **130**, 3:423-431.
14. Massart TJ, Peerlings RHJ, Geers MGD. An enhanced multi-scale approach for masonry wall computations with localizations of damage, Int. J. Numer. Meth. Engng 2007; **69:**1022-1059.
15. Chaboche JL, Feyel F, Monerie Y. Interface debonding models: a viscous regularization with a limited rate dependency, Int. J. Solid and Structures 2001; **38**:3127-3160.
16. Cristfield MA. Non-linear Finite Element Analysis of Solids and Structures. Vol. 1: Essential. John Wiley and Sons, 1997, Chichester, UK.
17. Simo JC, Hughes TJR. Computational Inelasticity: vol. 7 Interdisciplinary Applied Mathematics 1998, Springer, New York.
18. Zienkiewicz OC, Taylor RL. The finite element method. Vol. 1: The Basis. Fifth edition 2000. Butterworth-Heinemann.
19. Zienkiewicz OC, Taylor RL. The finite element method. Vol. 1: Solid Mechanics. Fifth edition 2000. Butterworth-Heinemann.
20. Izzuddin BA. An enhanced co-rotational approach for large displacement analysis of plates, Int. J. Numer. Meth. Engrg 2005; **64**:1350-1374.
21. Schellekens JCJ, de Borst R. On the numerical integration of interface elements, Int. J. Numer. Meth. Engrg 1993; **36**:43-66.
22. Point N, Sacco E. A delamination model for laminate composites. Int. J Solids and Struct. 1996; **33**(4):483-509.

23. Chaimoon K, Attard MM. Modelling of unreinforced masonry wall under shear and compression, Comp. and Struct. 2007; **29**:2056-2068.
24. Caballero A, Willam KJ, Carol I. Consistent tangent formulation for 3D interface modelling of cracking/fracture in quasi-brittle materials, Comput. Methods Appl. Mech. Engrg. 2008; **197**:2804-2822.
25. Hilsdorf HK. Investigation into the failure mechanism of brick masonry loaded in axial compression. In: Proceeding of designing, engineering and construction with Masonry products. Houston, USA, Gulf publishing company 1969; 34-14.
26. Rots JG. (Ed). Structural Masonry: An Experimental/Numerical Basis for Practical Design Rules, A.A. Balkema 1997, Rotterdam, the Netherlands.
27. Pérez-Foguet A, Rodriguez-Ferran A, Huerta A. Consistent tangent matrices for substepping schemes, Comput. Methods Appl. Mech. Engrg. 2000; **190**:4627-4647.
28. Izzuddin BA. Nonlinear Dynamic Analysis of Framed Structures, PhD Thesis, Imperial College, 1991.
29. Vermeltfoort AT, Raijmakers TMJ. Deformation controlled meso shear tests on masonry piers – Part.2, Draft Report, TU Eindhoven, dept. BKO, 1993.
30. Bean Popehn JR., Shultz AE, Lu M., Stolarski HK, Ojard NJ. Influence of transverse loading on the stability of slender unreinforced masonry walls, Engrg Struct. 2008; **30**:2830-2839.
31. Chee Liang NG. Experimental and theoretical investigation of the behavior of brickwork cladding panel subjected to lateral loading, PhD Thesis, University of Edinburgh, 1996.

Table 1. Initial values and primary variables for material parameters.

	F_1, Q_1			F_2, Q_2		
	C, C_Q	σ_t	$tan\phi$, $tan\phi_Q$	D	σ_c	$tan\theta$
Evolution law	Eq. (28)	Eq. (28)	Eq. (29)	Eq. (28)	Eq. (29)	Eq. (29)
Initial parameters and variables	A=C, C_Q A_0=C_0, C_{Q0} W_*=W_{pl1} G_*=$G_{f,II}$	A=σ_t A_0=σ_{t0} W_*=W_{pl1} G_*=$G_{f,I}$	B=$tan\phi$, $tan\phi_Q$ B_0=$tan\phi_0$, $tan\phi_{Q0}$ B_r=$tan\phi_r$, $tan\phi_{Qr}$ W_*=W_{pl1} G_*=$G_{f,I}$	A=D A_0=D_0 W_*=W_{pl2} G_*=G_c	B= σ_c B_0=σ_{c0} B_r=σ_{cr} W_*=W_{pl2} G_*=G_c	B=$tan\theta$ B_0=$tan\theta_0$ B_r= $tan\theta_r$ W_*=W_{pl2} G_*=G_c

Table 2. Mechanical properties of nonlinear interface elements for J4D/J5D walls [29].

	Elastic properties	Surface F_1	Surface Q_1	Surfaces F_2, Q_2
Mortar	k_n = 82 N/mm^3 k_t = 36 N/mm^3	σ_{t0} =0.25 MPa C_0 =0.375 MPa $tan\phi_0$ =0.75 $tan\phi$ = 0.75 $G_{f,I}$ =0.018 N/mm $G_{f,II}$ =0.125 N/mm	σ_{t0} =0.25 MPa C_0 =37.5 MPa $tan\phi_0$ =0.001 $tan\phi$ = 0.0001	σ_{c0} =10.5 MPa σ_{cr} =1.5 MPa D =10.5 MPa $tan\theta_0$ =0.045 $tan\theta_0$ =0.045 G_c = 5.0 N/mm
Brick	k_n = 1.0·10^{4}N/mm^3 k_t = 1.0·10^{4}N/mm^3	σ_{t0} =2.0 MPa C_0 =2.8 MPa $tan\phi_0$ =1.0 $tan\phi$ = 1.0 $G_{f,I}$ =0.08 N/mm $G_{f,II}$ =0.5 N/mm	σ_{t0} =2.0 MPa C_0 =2.8 MPa $tan\phi_0$ =1.0 $tan\phi$ = 1.0 $G_{f,I}$ =0.08 N/mm $G_{f,II}$ =0.5 N/mm	

Table 3. Mechanical properties of nonlinear interface elements for J7D wall [29].

	Elastic properties	Surface F_1	Surface Q_1	Surfaces F_2, Q_2
Mortar	k_n = 82 N/mm^3 k_t = 36 N/mm^3	σ_{t0} =0.16 MPa C_0 =0.224 MPa $tan\phi_0$ =0.75 $tan\phi$ = 0.75 $G_{f,I}$ =0.018 N/mm $G_{f,II}$ =0.05 N/mm	σ_{t0} =0.16 MPa C_0 =22.4 MPa $tan\phi_0$ =0.001 $tan\phi$ = 0.0001	σ_{c0} =11.5 MPa σ_{cr} =1.5 MPa D =11.5 MPa $tan\theta_0$ =0.045 $tan\theta_0$ =0.045 G_c = 5.0 N/mm
Brick	k_n = 1.0·10^{4}N/mm^3 k_t = 1.0·10^{4}N/mm^3	σ_{t0} =2.0 MPa C_0 =2.8 MPa $tan\phi_0$ =1.0 $tan\phi$ = 1.0 $G_{f,I}$ =0.08 N/mm $G_{f,II}$ =0.5 N/mm	σ_{t0} =2.0 MPa C_0 =2.8 MPa $tan\phi_0$ =1.0 $tan\phi$ = 1.0 $G_{f,I}$ =0.08 N/mm $G_{f,II}$ =0.5 N/mm	

Table 4. Mechanical properties of nonlinear interface elements for B1-25 wall [30].

	Elastic properties	Surface F_1	Surface Q_1	Surfaces F_2, Q_2
Mortar	k_n = 120 N/mm^3 k_t = 80 N/mm^3	σ_{t0} =0.124 MPa C_0 =0.21 MPa $tan\phi_0$ =0.58 $tan\phi$ = 0.58 $G_{f,I}$ =0.02 N/mm - N/mm $G_{f,II}$ =0.05 N/mm	σ_{t0} =0.124 MPa C_0 =0.21 MPa $tan\phi_0$ =0.001 $tan\phi$ = 0.0001	σ_{c0} =32.5 MPa σ_{cr} =0.0 MPa D = 10.0 MPa $tan\theta_0$ =0.005 $tan\theta_0$ =0.005 G_c = 5.0 N/mm
Brick	k_n = 1.0·10^{4}N/mm^3 k_t = 1.0·10^{4}N/mm^3	σ_{t0} =2.0 MPa C_0 =2.8 MPa $tan\phi_0$ =1.0 $tan\phi$ = 1.0 $G_{f,I}$ =0.08 N/mm $G_{f,I}$ =0.5 N/mm	σ_{t0} =2.0 MPa C_0 =2.8 MPa $tan\phi_0$ =1.0 $tan\phi$ = 1.0	

Table 5. Mechanical properties of nonlinear interface elements for wall tested by Chee Liang *et al.* [31].

	Elastic properties	Surface F_1	Surface Q_1	Surfaces F_2, Q_2
Mortar	k_n = 250 N/mm^3 k_t = 105 N/mm^3	σ_{t0} =0.35 MPa C_0 =0.42 MPa $tan\phi_0$ =0.57 $tan\phi$ = 0.57 $G_{f,I}$ =0.018 N/mm - 0.036 N/mm $G_{f,II}$ =0.125 N/mm	σ_{t0} =0.35 MPa C_0 =42.0 MPa $tan\phi_0$ =0.001 $tan\phi$ = 0.0001	σ_{c0} =6.0 MPa σ_{cr} =0.0 MPa D = 6.0 MPa $tan\theta_0$ =0.045 $tan\theta_0$ =0.045 G_c = 5.0 N/mm
Brick	k_n = 1.0·10^{4}N/mm^3 k_t = 1.0·10^{4}N/mm^3	σ_{t0} =1.0 MPa C_0 =1.2 MPa $tan\phi_0$ =1.0 $tan\phi$ = 1.0 $G_{f,I}$ =0.08 N/mm $G_{f,I}$ =0.5 N/mm	σ_{t0} =1.0 MPa C_0 =1.2 MPa $tan\phi_0$ =1.0 $tan\phi$ = 1.0	

List of figures

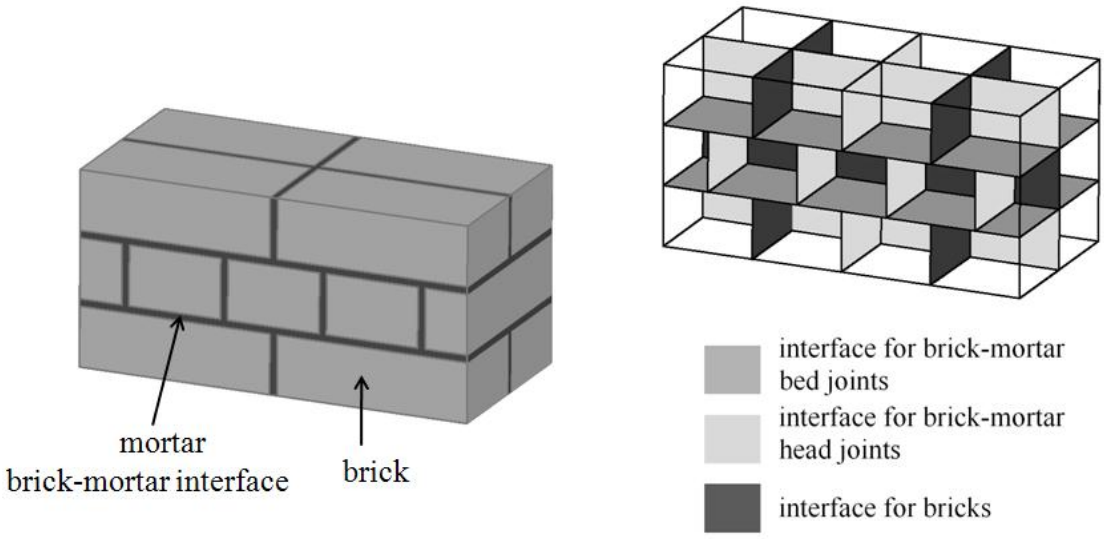

Figure 1. Interface elements for modelling brick-masonry.

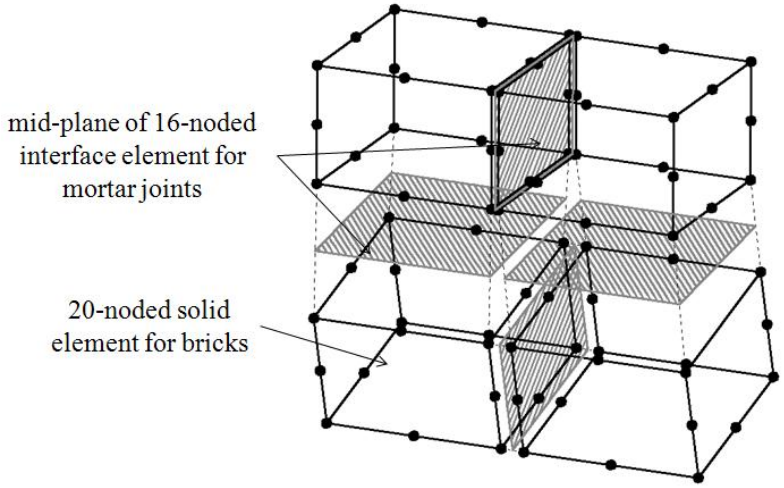

Figure 2. 3D mesoscale modelling for brick-masonry with 20-noded solid elements and 2D nonlinear interfaces.

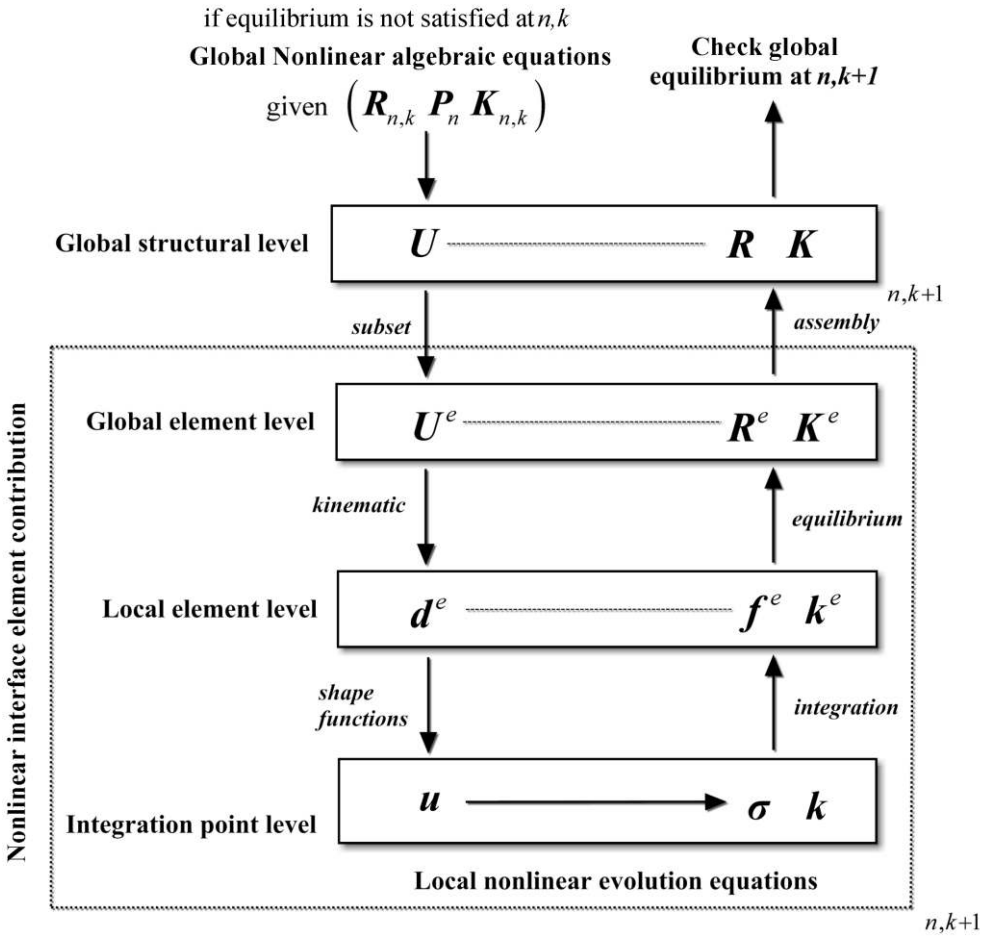

Figure 3. Solution procedure for the mesoscale modelling approach.

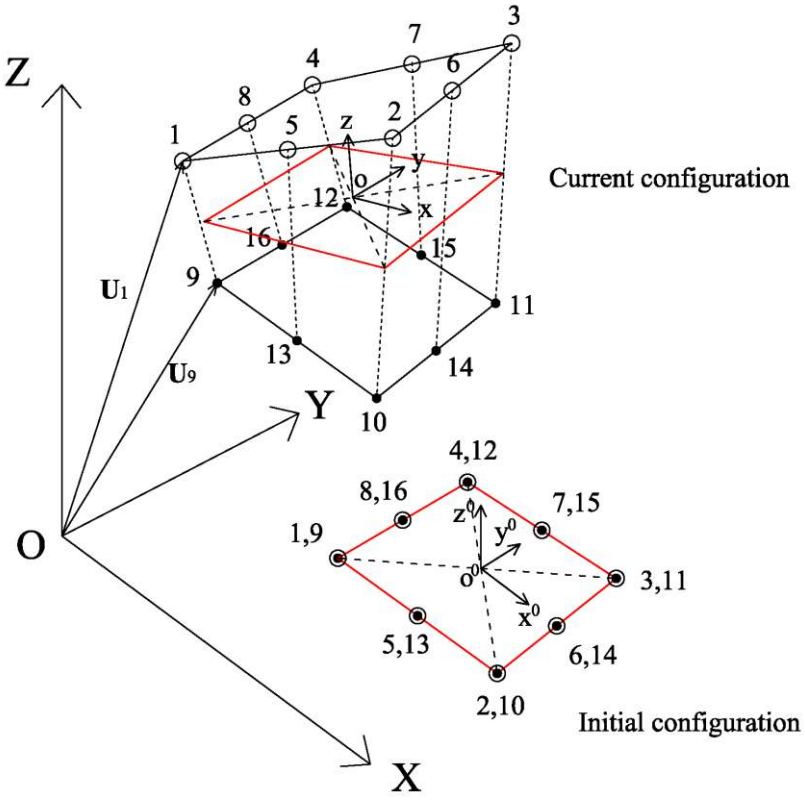

Figure 4. Global and local co-rotational systems.

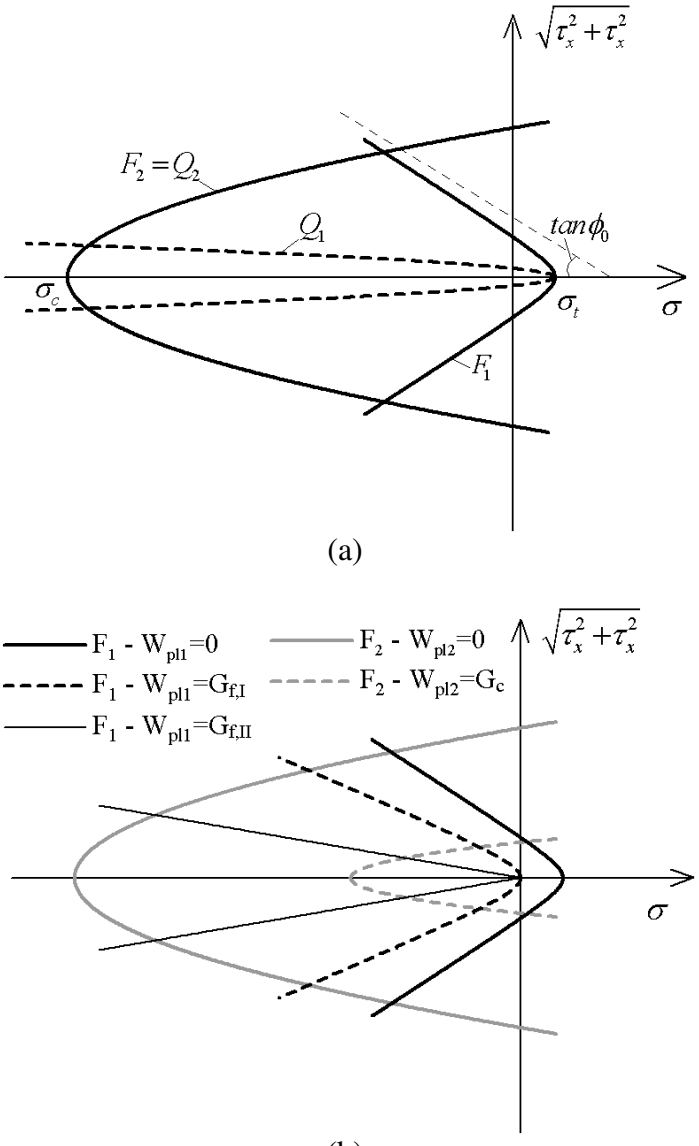

Figure 5. (a) Initial plastic surfaces and potentials, (b) evolution of plastic surfaces.

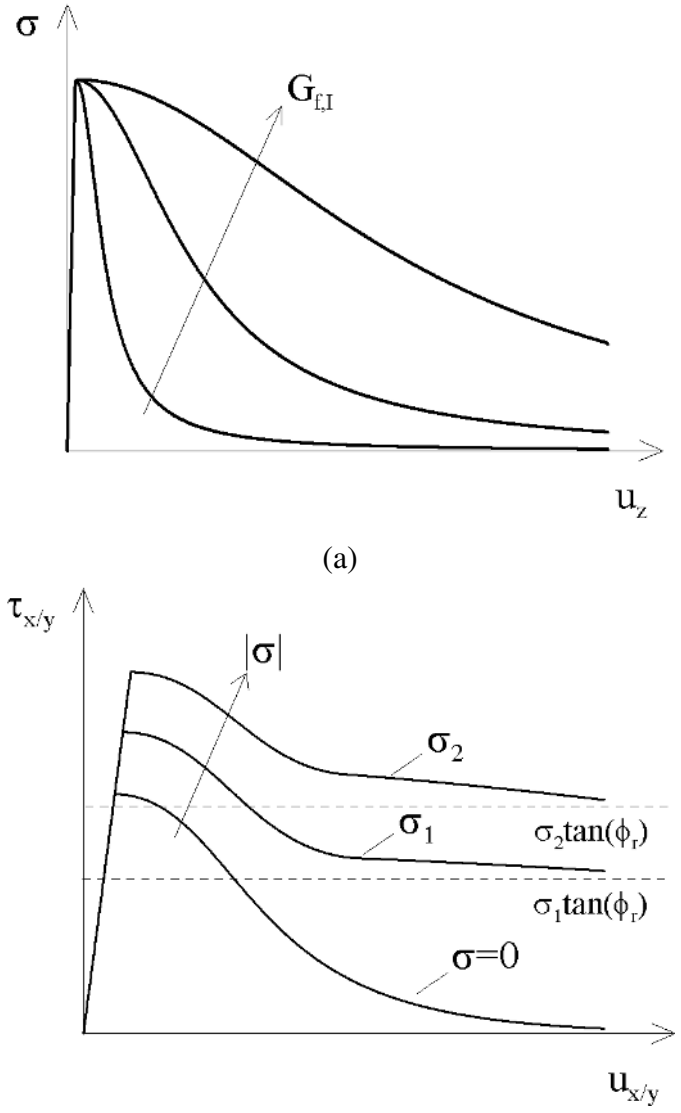

Figure 6. Traction deformation response: (a) tension, (b) shear.

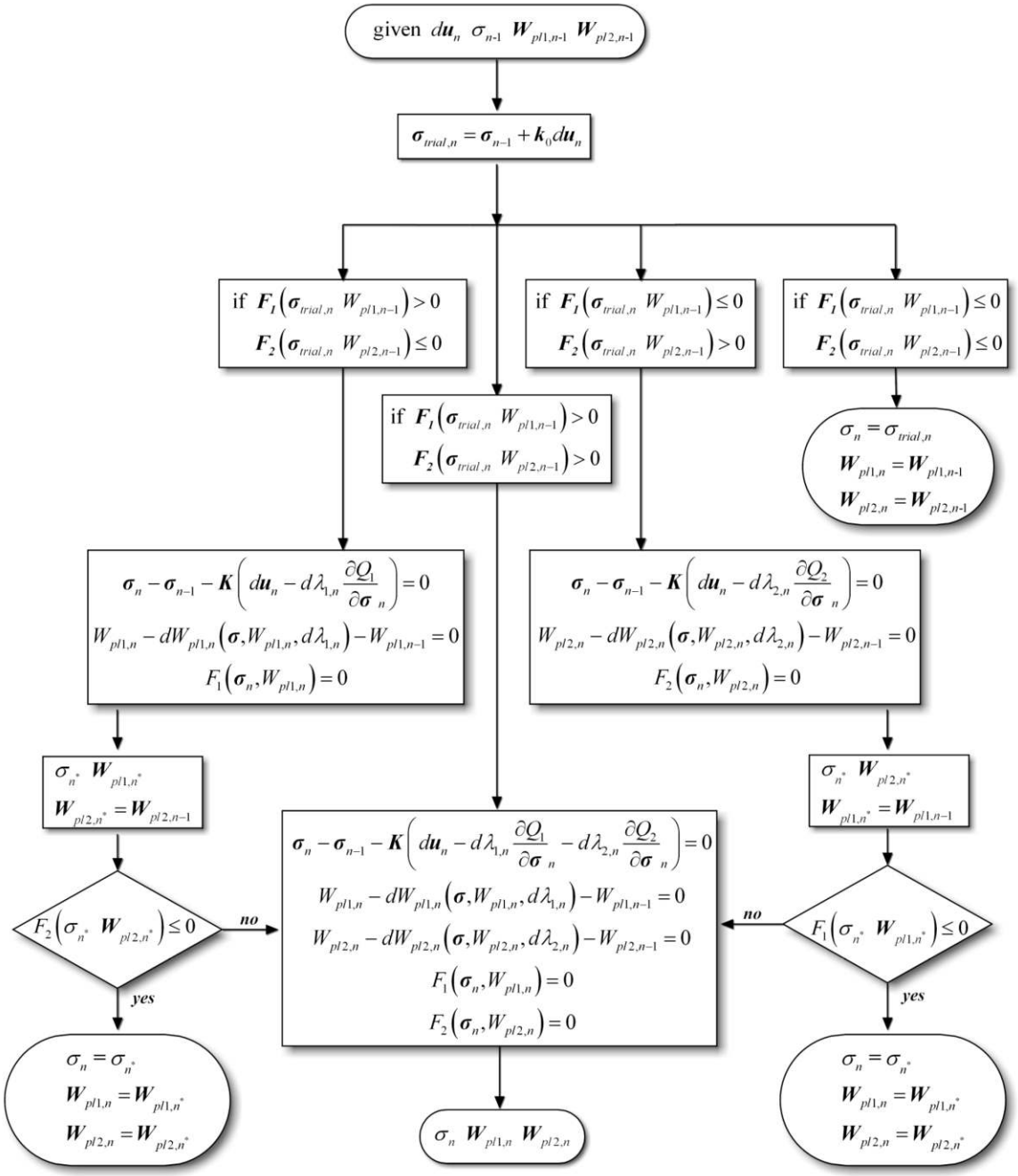

Figure 7. Solution procedure for the local plasticity problem at quadrature point level.

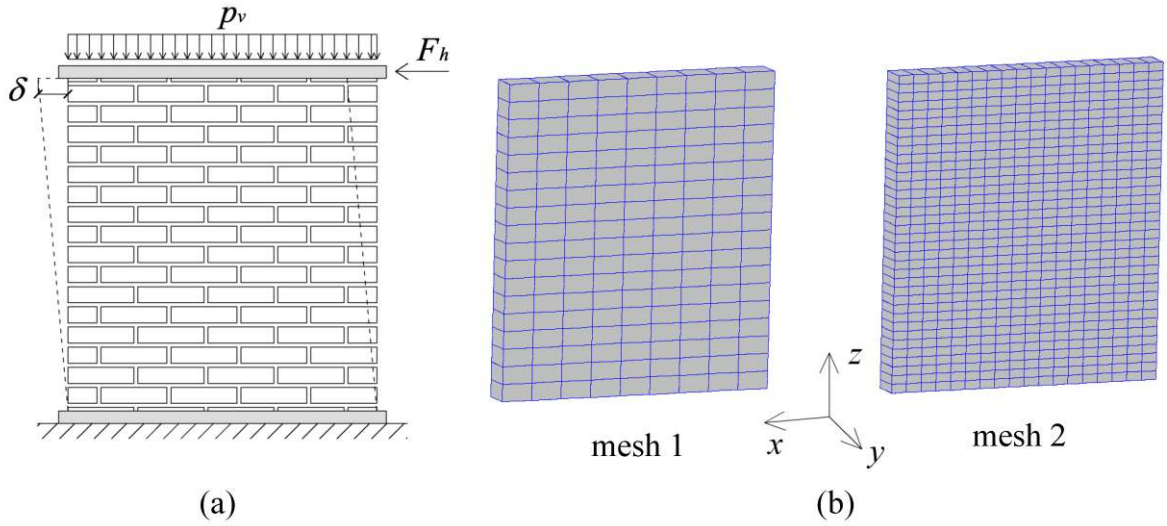

Figure 8. URM wall loaded in plane: (a) boundary conditions [29], (b) employed meshes.

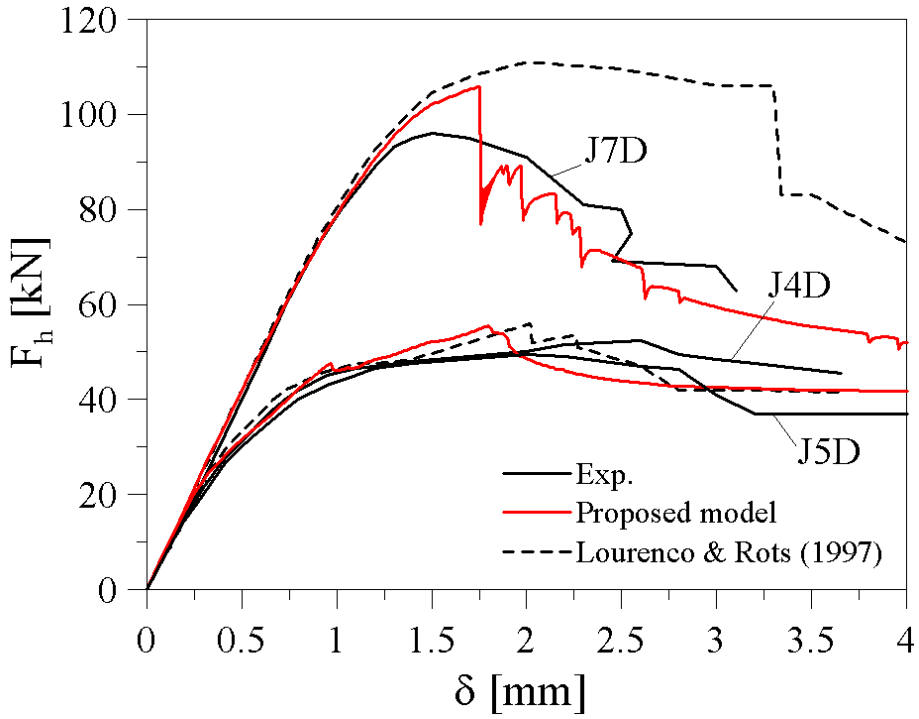

Figure 9. Experimental-numerical comparisons for the URM wall loaded in plane.

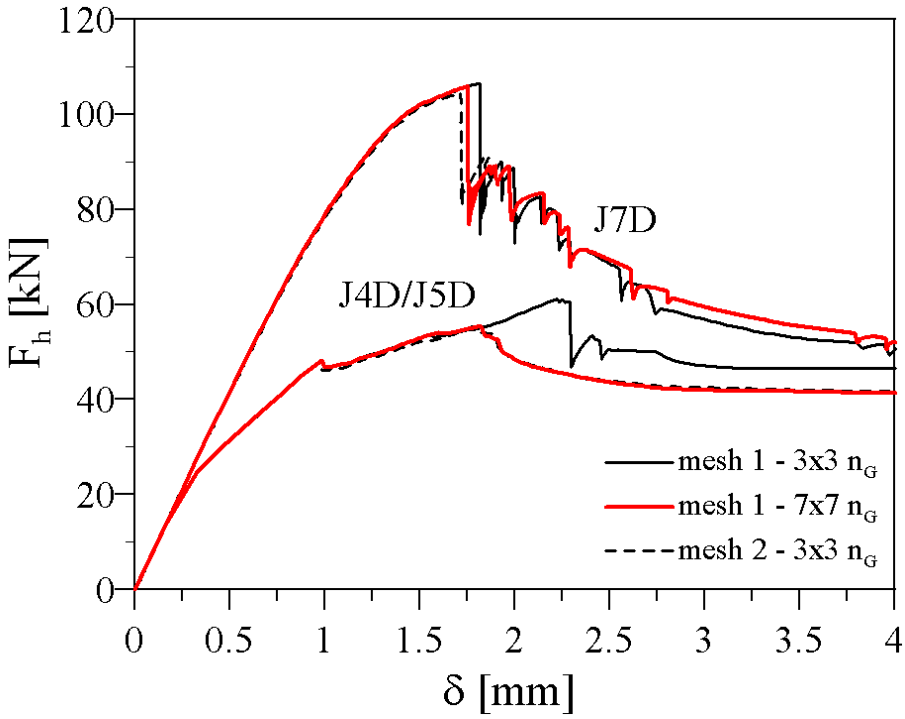

Figure 10. Numerical comparisons for the wall loaded in-plane: influence of mesh refinement and integration points.

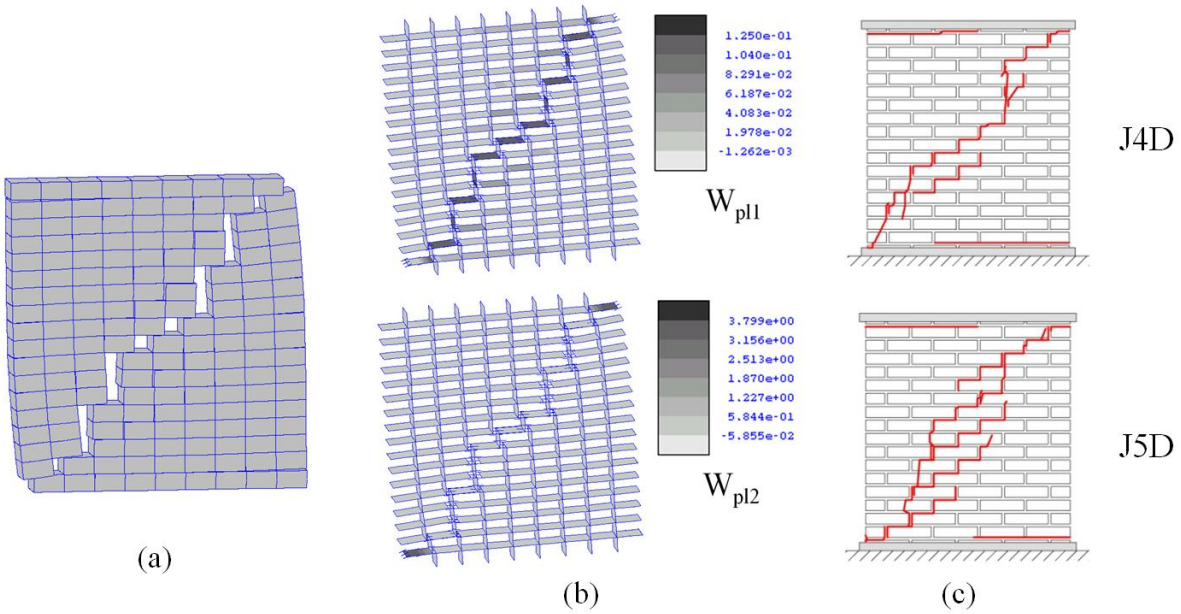

Figure 11. Wall loaded in-plane: (a) deformed shape (displacement scale=20) and (b) plastic work contours at collapse, (c) cracks paths surveyed after the tests [29].

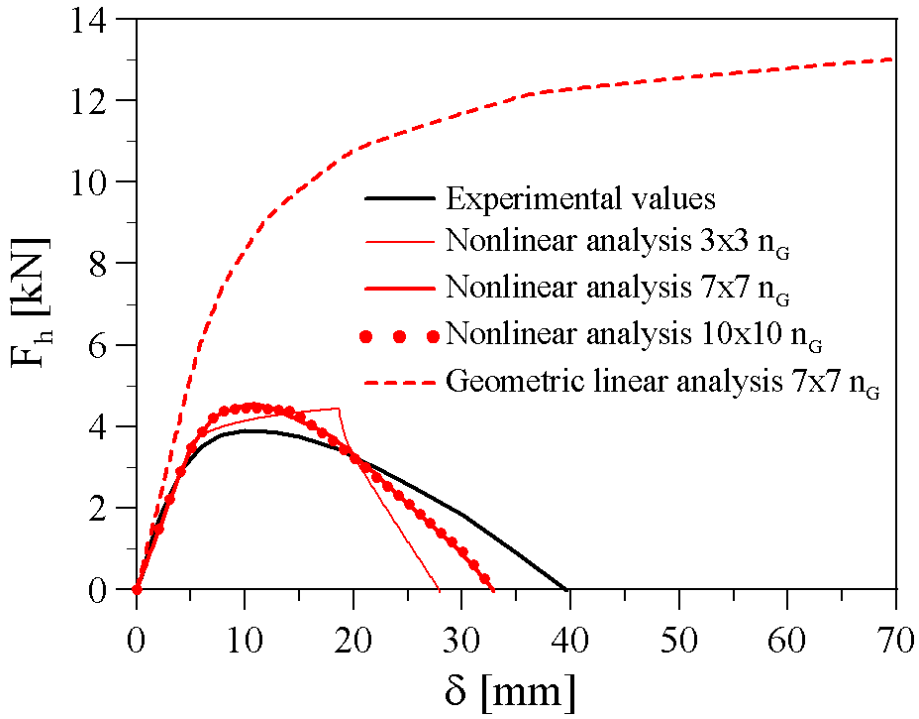

Figure 12. Experimental-numerical comparison for the URM wall B1-25 loaded out-of-plane.

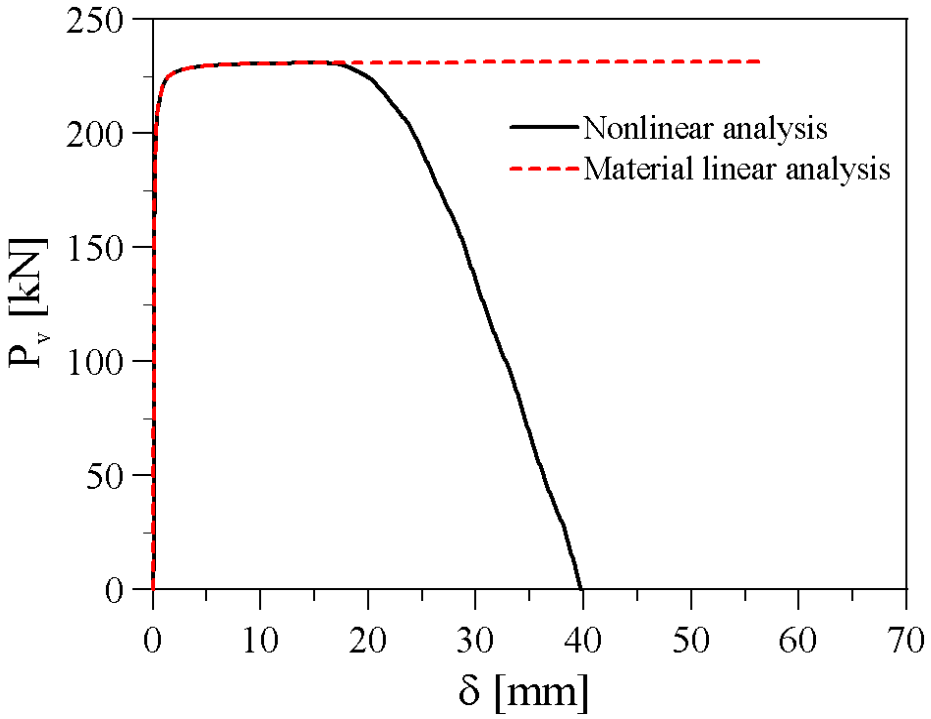

Figure 13. Buckling load for the URM wall B1-25.

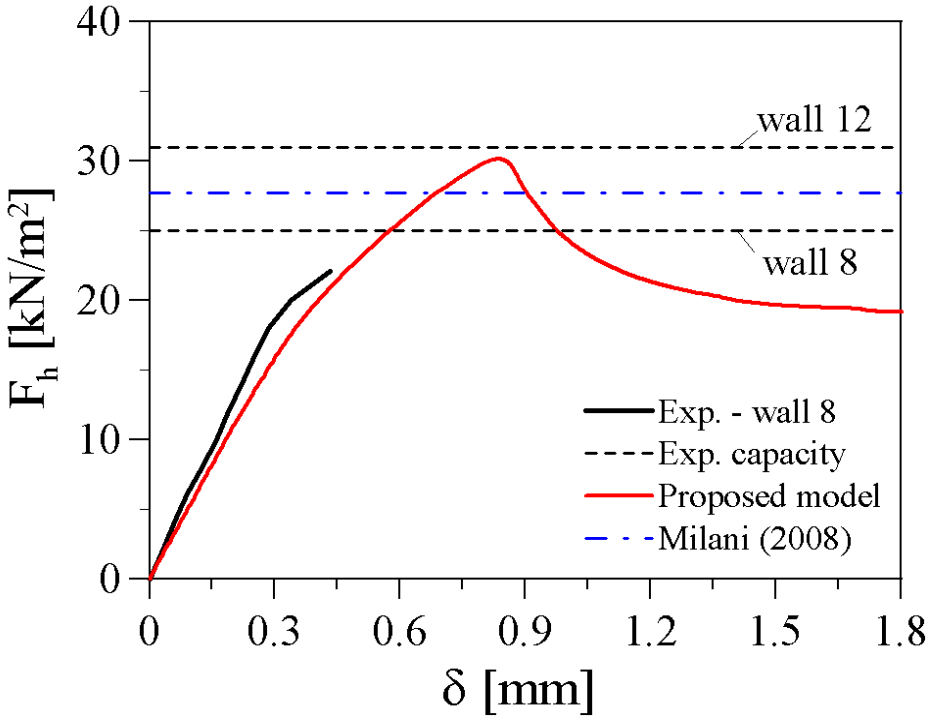

Figure 14. Wall loaded out-of-plane [30]: numerical-experimental comparisons.

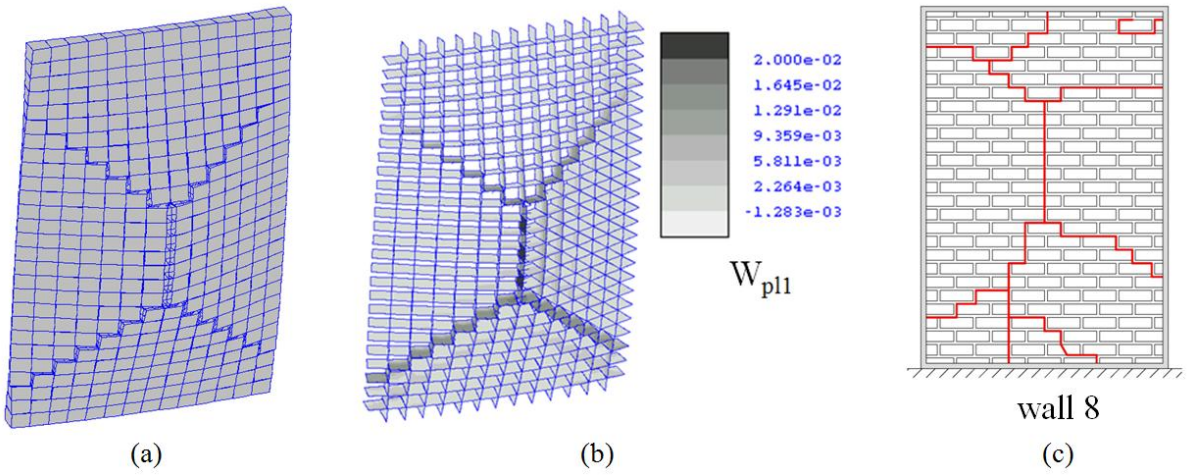

Figure 15. Wall loaded out-of-plane : (a) deformed shape (displacement scale=100) and (b) plastic work contours at the end of the analysis, (c) cracks paths surveyed after the test [30].